



VRIJE  
UNIVERSITEIT  
BRUSSEL

<sup>1</sup> **A search for flavour changing neutral currents  
2 involving a top quark and a Z boson, using the  
3 data collected by the CMS collaboration at a  
4 centre of mass of 13 TeV**

<sup>5</sup> Van Parijs, Isis

<sup>6</sup> Proefschrift ingediend met het oog op het behalen van de academische graad  
<sup>7</sup> Doctor in de Wetenschappen.

Published in Faculteit Wetenschappen & Bio-ingenieurswetenschappen  
Vrije Universiteit Brussel  
At 1. June 2017.

<sup>8</sup>

Responsible Contact: I. Van Parijs  
Institute for High Energy Physics  
Promotor: Prof. Jorgen D'Hondt

9      First Referee:                            Prof. Dr. J. D'Hondt  
            Date of Hand-in:                        10 November 2017  
            Date of Defense:                        10 December 2017

# Contents

---

11	<b>1 An introduction to the theory</b>	1
12	1.1 Elementary particles and forces . . . . .	1
13	1.2 Standard Model Lagrangian . . . . .	2
14	1.3 Flavour changing currents in the SM . . . . .	5
15	1.4 Top quark physics in the SM . . . . .	6
16	1.5 Motivations for new physics . . . . .	9
17	1.6 An effective approach beyond the SM: FCNC involving a top quark . . . . .	11
18	1.7 Experimental constraints on top-FCNC . . . . .	12
19	<b>2 Experimental set-up</b>	15
20	2.1 The Large Hadron Collider . . . . .	15
21	2.2 The Compact Muon Solenoid . . . . .	18
22	2.2.1 CMS coordinate system . . . . .	20
23	2.2.2 Towards the heart of CMS . . . . .	20
24	2.2.3 Data acquisition . . . . .	31
25	2.2.4 CMS computing model . . . . .	32
26	<b>3 Analysis techniques</b>	33
27	3.1 Hadron collisions at high energies . . . . .	33
28	3.2 Event generation . . . . .	36
29	3.2.1 Fundamentals of simulating a proton collision . . . . .	36
30	3.2.2 Programs for event generation . . . . .	37
31	3.2.3 Generating FCNC top-Z interactions . . . . .	38
32	3.2.4 Generating SM background events . . . . .	39
33	3.3 Multivariate analysis techniques: Boosted Decision Trees . . . . .	42
34	3.4 Template-based fitting . . . . .	44
35	<b>4 Event reconstruction and selection</b>	45
36	4.1 Event reconstruction . . . . .	45
37	4.2 Event selection . . . . .	45
38	4.3 Regions and channels . . . . .	45
39	4.4 Data driven background simulation . . . . .	45
40	<b>5 The search for FCNC involving a top quark and a Z boson</b>	47

41	5.1 Construction of template distributions . . . . .	47
42	5.2 Systematic uncertainties . . . . .	47
43	5.3 Limit setting procedure . . . . .	47
44	5.4 Result and discussion . . . . .	47
45	<b>6 Conclusion and outlook</b>	<b>49</b>
46	<b>Bibliography</b>	<b>51</b>

# Theoretical basis

# 1

48 The Standard Model (SM) [1] is a name given in 1970s to a theory describing the fundamental  
 49 particles and their interactions. This quantum field theory describes the particles and their  
 50 interactions as fields and has successfully incorporated three of the four fundamental forces in  
 51 the universe. In [Section 1.1](#), the particle content of the SM is summarised, while [Section 1.2](#)  
 52 describes the SM Lagrangian and its symmetries. In [Section 1.3](#), the flavour content of the SM  
 53 is highlighted.

54 The successful theory of the SM has some shortcomings which are discussed in [Section 1.5](#)  
 55 and lead to searches for a more general theory. One of such a search is using effective field  
 56 theory (EFT) [2] to search for new physics in a model independent way. In [Section 1.6](#) an EFT  
 57 model focussing on flavour changing neutral currents (FCNC) involving a top quark is presented.  
 58 Its current experimental constraints are given in [Section 1.7](#).

## 59 1.1 Elementary particles and forces

60 The interactions in nature can be described by four forces, the strong force, the electromagnetic  
 61 (EM) force, the weak force and the gravitational force. These interactions happen via particles  
 62 with an integer spin known as bosons. The strong interaction is mediated by eight gluons  $g$ ,  
 63 while the electromagnetic force is mediated by photons  $\gamma$ , and the weak force by  $Z$  and  $W^\pm$   
 64 bosons. In [Table 1.1](#), the forces and their characteristics are shown. The gravitational force is  
 65 the only force not included in the SM and can be neglected for energies lower than the Planck  
 scale ( $1.22 \cdot 10^{19}$  GeV).

**Table 1.1:** The four forces of nature and their characteristics.

	Range	Mediator
Strong force	$10^{\text{-}e} - 15$ m	8 gluons
Electromagnetic force	$\infty$	photon
Weak force	$10^{\text{-}18}$ m	$W^\pm$ , Z bosons
Gravitational force	$\infty$	unknown

67 The fermions are the particles that make up the visible matter in the universe. They carry  
 68 half integer spin and can be subdivided into leptons and quarks, where leptons don't interact  
 69 strongly. Each fermion has a corresponding anti-fermion which has the same mass and is  
 70 oppositely charged. The electron  $e^-$  is the first elementary particle discovered [3] and belongs  
 71 to the first generation of leptons together with the electron neutrino  $\nu_e$ . The second generation  
 72 compromises the muon  $\mu^-$  and muon neutrino  $\nu_\mu$ , whereas the third generation consists of  
 73 the tau  $\tau$  and tau neutrino  $\nu_\tau$ . The neutrino's are neutral particles, while the other leptons  
 74 have charge  $\pm q_e$  where  $q_e$  represents the elementary charge of  $1.602 \cdot 10^{-19}$  C. The masses of  
 75 charged leptons differ by four orders of magnitude between the first and third generations. In  
 76 the SM the neutrino's are assumed to be massless, nonetheless it is experimentally established  
 77 that neutrino do have a tiny non-zero mass. In Table 1.2, the leptons and their properties in the  
 SM are summarised.

**Table 1.2:** The properties of the leptons in the three generations of the SM [4], where  $q_e$  represents the elementary charge.

Generation	Particle	Mass	Charge
First	$e^-$	0.511 MeV	$-q_e$
	$\nu_e$	$\approx 0$	0
Second	$\mu^-$	106 MeV	$-q_e$
	$\nu_\mu$	$\approx 0$	0
Third	$\tau$	1 777 MeV	$-q_e$
	$\nu_\tau$	$\approx 0$	0

78

79 The quarks can also be divided into three generations. Unlike the leptons, they carry colour  
 80 charge and can interact via the strong interaction. The top quark, discovered in 1995 at the  
 81 Tevatron [5, 6], is the heaviest SM particle with a mass close to  $173.1 \pm 0.6$  GeV<sup>1</sup> [4]. The quarks  
 82 and their properties are summarized in Table 1.3. In nature, only colour neutral objects can exist.  
 83 This has as consequence that quarks are bound through gluons into mesons (quark+anti-quark)  
 84 and baryons (three quarks). These mesons and baryons are mostly short-lived and unstable  
 85 particle that rapidly decay through  $W^\pm$  and Z bosons, associated with a fermion. The only  
 86 known stable baryon is the proton, made up of two up quarks and one down quark.

87 The scalar boson, commonly known as the Higgs boson, is the last piece of the SM and is  
 88 discovered in 2012 [7, 8]. It is responsible for the masses of the  $W^\pm$  and Z boson, and that of  
 89 the fermions.

## 90 1.2 Standard Model Lagrangian

91 The SM is a quantum field theory and thus describes the dynamics and kinematics of particles  
 92 and forces by a Lagrangian  $\mathcal{L}$ . The theory is based on the  $SU_C(3) \times SU_L(2) \times U_Y(1)$  gauge  
 93 symmetry, where  $SU_L(2) \times U_Y(1)$  describes the electroweak interaction and  $SU_C(3)$  the strong

---

<sup>1</sup>In this thesis all masses and energies are expressed in natural units, where the speed of light and  $\hbar$  are taken to be equal to one.

**Table 1.3:** The properties of the quarks in the three generations of the SM [4], where  $q_e$  represents the elementary charge.

	Generation	Particle	Mass	Charge
First	up u	$2.2^{+0.6}_{-0.4}$ MeV	$\frac{2}{3} q_e$	
	down d	$4.7^{+0.5}_{-0.4}$ MeV	$\frac{-1}{3} q_e$	
Second	charm c	$1.28 \pm 0.03$ GeV	$\frac{2}{3} q_e$	
	strange s	$96^{+8}_{-4}$ MeV	$\frac{-1}{3} q_e$	
Third	top t	$173.1 \pm 0.6$ GeV	$\frac{2}{3} q_e$	
	bottom b	$4.18^{+0.04}_{-0.03}$ GeV	$\frac{-1}{3} q_e$	

coupling. The indices refer to colour C, the left chiral nature of the  $SU_L(2)$  coupling L, and the weak hypercharge Y. Its Lagrangian is constructed such that contains symmetries representing physics conservation laws such as conservation of energy, momentum and angular momentum. The symmetries under local group transformations are sustained by demanding gauge invariance .

The  $U_Y(1)$  group has one generator Y with an associated gauge field  $B_\mu$ . The three gauge fields  $W_\mu^1$ ,  $W_\mu^2$ , and  $W_\mu^3$ , are associated to  $SU_L(2)$  with three generators that can be written as half of the Pauli matrices:

$$T_1 = \frac{1}{2} \begin{pmatrix} 0 & 1 \\ 1 & 0 \end{pmatrix}, \quad T_2 = \frac{1}{2} \begin{pmatrix} 0 & -i \\ i & 0 \end{pmatrix}, \quad \text{and} \quad T_3 = \frac{1}{2} \begin{pmatrix} 1 & 0 \\ 0 & -1 \end{pmatrix}. \quad (1.1)$$

The generators  $T^a$  satisfy the Lie algebra:

$$[T^a, T^b] = i\epsilon^{abc} T_c \text{ and } [T^a, Y] = 0, \quad (1.2)$$

where  $\epsilon^{abc}$  is an antisymmetric tensor. The gauge fields of  $SU_L(2)$  only couple to left-handed fermions as required by the observed parity violating nature of the weak force. The  $SU_C(3)$  group represents quantum chromodynamics (QCD). It has eight generators corresponding to eight gluon fields  $G_\mu^{1..8}$ . Unlike  $SU_L(2) \times U_Y(1)$ ,  $SU_C(3)$  is not chiral.

Under  $SU_C(3)$  quarks are colour triplets while leptons are colour singlets. This implies that the quarks carry a colour index ranging between one and three, whereas leptons do not take part in strong interactions. Based on the chirality, the quarks and leptons are organized in doublets or singlets. Each generation  $i$  of fermions consists of left-handed doublets and right-handed singlets:

$$l_{L,i} = \begin{pmatrix} e^-_{L,i} \\ \nu_{L,i} \end{pmatrix}, \quad e^-_{R,i}, \quad q_{L,i} = \begin{pmatrix} u_{L,i} \\ d_{L,i} \end{pmatrix}, \quad u_{R,i}, \quad \text{and} \quad d_{R,i} \quad (1.3)$$

The SM Lagrangian can be decomposed as a sum of four terms

$$\mathcal{L}_{SM} = \mathcal{L}_{gauge} + \mathcal{L}_f + \mathcal{L}_{Yuk} + \mathcal{L}_\phi, \quad (1.4)$$

**NOTE:**  
should I explain gauge invariance or is a reference enough?

that are related to the gauge, fermion, Yukawa and scalar sectors. The gauge Lagrangian regroups the gauge fields of all three symmetry groups, and the fermionic part consists of kinetic energy terms for quarks and leptons. The interaction between fermions and the scalar doublet  $\phi$  gives rise to fermion masses and is described by the Yukawa Lagrangian. The scalar part of the Lagrangian is composed of a kinematic and potential component related to the scalar boson.

For the electroweak theory, two coupling constants are introduced, namely  $g'$  for  $U_Y(1)$  and  $g$  for  $SU_L(2)$ . The physically observable gauge bosons of this theory are the photon field  $A_\mu$ , the Z boson field  $Z_\mu^0$ , and the W field  $W_\mu^\pm$ . These are a superposition of the four gauge fields of  $SU_L(2) \times U_Y(1)$ :

$$A_\mu = \sin\theta_W W_\mu^1 + \cos\theta_W B_\mu, \quad Z_\mu^0 = \cos\theta_W W_\mu^3 - \sin\theta_W B_\mu, \quad \text{and} \quad W_\mu^\pm = \sqrt{\frac{1}{2}} (W_\mu^1 \mp W_\mu^2), \quad (1.5)$$

where  $\theta_W$  represents the weak mixing angle defined as  $\tan\theta_W = \frac{g'}{g}$ .

The coupling constant representing the strength of the QCD interactions is denoted as  $g_s$ . In QCD there is asymptotic freedom whereby the strong coupling constant becomes weaker as the energy with which the interaction between strongly interacting particles is probed increases, and stronger as the distance between the particles increases. A consequence of this is known as colour confinement. The quarks and gluons can not exist on their own and are not observed individually. They are bound in colour neutral states called hadrons, this process is known as hadronisation.

## 116 Electroweak symmetry breaking

In  $\mathcal{L}_{\text{gauge}}$  and  $\mathcal{L}_f$  are no mass terms for fermions present because only singlets under  $SU_C(3) \times SU_L(2) \times U_Y(1)$  can acquire a mass with an interaction of the type  $m^2 \phi^\dagger \phi$  without breaking the gauge invariance. In order to accommodate mass terms for fermions and gauge fields, electroweak symmetry breaking, leading to  $\mathcal{L}_\phi$  is introduced.

The scalar doublet is introduced in the SM as

$$\phi = \frac{1}{\sqrt{2}} \begin{pmatrix} \varphi_1 + i\varphi_2 \\ \varphi_3 + i\varphi_4 \end{pmatrix}. \quad (1.6)$$

**NOTE:**  
check if I  
need to add  
constants  
here

Its field potential is of the form

$$V(\phi) = \mu^2 \phi^\dagger \phi + \lambda (\phi^\dagger \phi)^2, \quad (1.7)$$

with  $\mu^2 < 0$  and  $\lambda$  a positive integer. This choice of parameters gives the potential a "Mexican hat" shape. It has an infinite set of minima (ground states) and by expanding the field around an arbitrary choice of ground state, the electroweak symmetry is broken (EW):

$$\phi = \begin{pmatrix} 0 \\ \frac{v}{\sqrt{2}} \end{pmatrix} + \hat{\phi}, \quad (1.8)$$

where  $v$  is the vacuum expectation value (vev), measured to be around 245 GeV and corresponds to  $\sqrt{\frac{-\mu}{\lambda}}$ . The scalar doublet's four degrees of freedom is reduced to three degrees of freedom

that couple to the gauge fields and mix with the  $W^+$ ,  $W^-$  and  $Z$  bosons. The remaining fourth degree of freedom has given rise to a physically observable particle , called the Brout-Englert-Higgs (BEH) boson. This spontaneous symmetry breaking leaves the gauge invariance intact and gives masses to the  $W^\pm$  and  $Z$  bosons as:

$$m_W = \frac{1}{2}v|g| \quad \text{and} \quad m_Z = \frac{1}{2}v\sqrt{g'^2 + g^2}. \quad (1.9)$$

- 121 The Brout-Englert-Higgs field couples universally fermions with a strength proportional to their  
122 masses, and to gauge bosons with a strength proportional to the square of their masses.

### 123 1.3 Flavour changing currents in the SM

Flavour changing charged currents are introduced in 1963 by Nicola Cabibbo [9]. Via interaction with a  $W$  boson the flavour of the quarks is changed. At the time of the postulation only up, down, and strange quarks were known and the charged weak current was described as a coupling between the up quark and  $d_{\text{weak}}$ , where  $d_{\text{weak}}$  is a linear combination of the down and strange quarks,  $d_{\text{weak}} = \cos\theta_c d + \sin\theta_c s$ . This linear combination is a direct consequence of the chosen rotation

$$\begin{pmatrix} d_{\text{weak}} \\ s_{\text{weak}} \end{pmatrix} = \begin{pmatrix} \cos\theta_c & \sin\theta_c \\ -\sin\theta_c & \cos\theta_c \end{pmatrix} \begin{pmatrix} d \\ s \end{pmatrix} = \mathcal{R} \begin{pmatrix} d \\ s \end{pmatrix}, \quad (1.10)$$

where the rotation angle  $\theta_c$  is known as the Cabibbo angle. This provides a definition for the charged weak current between  $u$  and  $d$  quarks,

$$J_\mu = \bar{u} \gamma_\mu (1 + \gamma_5) d_{\text{weak}}. \quad (1.11)$$

A consequence of Cabibbo's approach is that the  $s_{\text{weak}}$  is left uncoupled, leading to Glashow, Iliopoulos and Maiani (GIM) [10–12] to require the existence of a fourth quark with charge  $\frac{2}{3}q_e$ . This quark, known as the charm quark, couples to  $s_{\text{weak}}$  and a new definition of the charged weak current is modified to

$$J_\mu = (u \ c) \gamma_\mu (1 + \gamma_5) \mathcal{R} \begin{pmatrix} d \\ s \end{pmatrix} = \bar{U} \gamma_\mu (1 + \gamma_5) \mathcal{R} D. \quad (1.12)$$

The neutral weak current is defined as

$$J_3 = \bar{U} \gamma_\mu (1 + \gamma_5) [\mathcal{R}, \mathcal{R}^\dagger] D, \quad (1.13)$$

- 124 and is diagonal in flavour space. This has as consequence that no flavour changing neutral  
125 currents occur at tree-level Feynmann diagrams<sup>2</sup>.

Kobayashi and Maskawa generalised the Cabibbo rotation matrix to accommodate for a third generation of quarks. The result is a  $3 \times 3$  unitary matrix known as the CKM matrix, responsible

**NOTE:**  
should I  
explain  
feynmann  
diagrams?

---

<sup>2</sup>Feynmann diagrams are physical representation of interaction between particles. They are based on Feynmann rules [1].

for the mixing of weak interaction states of down-type quarks:

$$\begin{pmatrix} d_{\text{weak}} \\ s_{\text{weak}} \\ b_{\text{weak}} \end{pmatrix} = \begin{pmatrix} V_{ud} & V_{us} & V_{ub} \\ V_{cd} & V_{cs} & V_{cb} \\ V_{td} & V_{ts} & V_{tb} \end{pmatrix} \begin{pmatrix} d \\ s \\ b \end{pmatrix} = \mathcal{V}_{\text{CKM}} \begin{pmatrix} d \\ s \\ b \end{pmatrix}. \quad (1.14)$$

The unitarity of the matrix ( $\mathcal{V}_{\text{CKM}}^\dagger \mathcal{V}_{\text{CKM}} = \mathbb{1}$ ). A general  $3 \times 3$  unitary matrix depends on three real angles and six phases. For the CKM matrix, the freedom to redefine the phases of the quark eigenstates can remove five of the phases, leaving a single physical phase known as the Kobayashi-Maskawa phase. This phase is responsible for the charge parity violation in the SM [13]. Each element  $V_{ij}$  of  $\mathcal{V}_{\text{CKM}}$  represents the transition probability of a quark  $i$  going to a quark  $j$ , and is experimentally determined to be [4]

$$\mathcal{V}_{\text{CKM}} = \begin{pmatrix} 0.97425 \pm 0.00022 & 0.2253 \pm 0.0008 & (4.13 \pm 0.49) 10^{-3} \\ 0.225 \pm 0.008 & 0.986 \pm 0.016 & (41.1 \pm 1.3) 10^{-3} \\ (8.4 \pm 0.6) 10^{-3} & (40.0 \pm 2.7) 10^{-3} & 1.021 \pm 0.032 \end{pmatrix}. \quad (1.15)$$

From Equation 1.15 follows that top quarks predominantly decay via charged weak currents to bottom quarks, with a probability consistent with unity. In the SM, FCNC can only occur via higher loop Feynmann diagrams which are highly suppressed. The expected transition probabilities for a top quark decaying via a FCNC interaction in the SM are given in Table 1.4, where it is clear that the FCNC sector of the SM is still beyond the reach of the sensitivity of current experiments.

**Table 1.4:** The predicted branching ratios  $\mathcal{B}$  for FCNC interactions involving the top quark in the SM [14]

Process	$\mathcal{B}$ in the SM	Process	$\mathcal{B}$ in the SM
$t \rightarrow uZ$	$8 \cdot 10^{-17}$	$t \rightarrow cZ$	$1 \cdot 10^{-14}$
$t \rightarrow u\gamma$	$4 \cdot 10^{-16}$	$t \rightarrow c\gamma$	$5 \cdot 10^{-14}$
$t \rightarrow ug$	$4 \cdot 10^{-14}$	$t \rightarrow cg$	$5 \cdot 10^{-12}$
$t \rightarrow uH$	$2 \cdot 10^{-17}$	$t \rightarrow cH$	$3 \cdot 10^{-15}$

131

## 1.4 Top quark physics in the SM

**NOTE:** Add source

Discovered in 1995 by the CDF and D0 collaborations at Tevatron with proton-antiproton data, the top quark plays an important role in studying high energy physics. Its Yukawa interaction is given by

$$\mathcal{L}_{\text{top-Yukawa}} = -\frac{\lambda_t}{\sqrt{2}} \bar{t}_L t_R - \frac{\lambda_t}{\sqrt{2}} \bar{H} \bar{t}_L t_R + \text{h.c.}, \quad (1.16)$$

yielding a Yukawa coupling of

$$\lambda_t = \frac{\sqrt{2} m_t}{v} = 0.991 \pm 0.003, \quad (1.17)$$

133 with the top mass  $m_t$  equal to  $172.44 \pm 0.49$  GeV [4]. This Yukawa coupling is very large  
 134 compared to the other Yukawa couplings in the SM  $\mathcal{O}(10^{-2})$ , leading to the belief that the top  
 135 quark may have an important role in understanding the mechanism of electroweak symmetry  
 136 breaking. On top of this, the very short lifetime of the top quark makes it an excellent candidate  
 137 for property studies. Its high mass, almost 40 times higher than the mass of the closest particle  
 138 in mass, leads to a large coupling with the Higgs boson and makes the top quark an interesting  
 139 candidate for the understanding of how particles acquire mass.

140 The CKM matrix element  $V_{tb}$ , given in [Equation 1.15](#), is experimentally found to be much  
 141 larger than  $V_{ts}$ ,  $V_{td}$ , and close to unity. The top quark decays through electroweak interactions  
 142 since the W boson mass is smaller than the top mass and the W boson can be on shell. A  
 143 consequence of this is that the top quark has a very short lifetime of only  $1/\Gamma_t \approx 5 \cdot 10^{-25}$  s leading  
 144 to the fact that the formation of bound states involving top quarks are not allowed. [This lifetime](#)  
 145 is even shorter than the typical hadronisation timescale of  $1/\Lambda_{QCD} \approx 10^{-23}$  s, prohibiting gluons  
 146 to radiate from the top quark and keeping its spin coherent. Since the electroweak interactions  
 147 have a V-A coupling structure, the top quark spin orientation can be derived from the angular  
 148 distributions of its decay products. This makes it possible to study the polarisation of top quarks  
 149 from the angular distributions in various processes.

**NOTE:** Add source

**NOTE:** Add source

150 The massiveness of the top quark leads to the fact that a large amount of energy is needed  
 151 to create one. This is only the case for high energy collisions such as those in the Earth's  
 152 upper atmosphere as cosmic rays collide with particles in air, or by particle accelerators. The  
 153 production of top quarks happens in two ways: single via the electroweak interaction or in  
 154 pairs via the strong interaction. At hadron colliders, the dominant production mechanism is top  
 155 quark production via gluon ( $gg \rightarrow t\bar{t}$ ) or quark fusion ( $q\bar{q} \rightarrow t\bar{t}$ ). In [Figure 1.1](#), the different top  
 156 pair production mechanisms are shown. The production channel of gluon fusion is the main  
 157 contributor to the top pair cross section at the LHC compared to quark fusion at Tevatron. The  
 158  $gg \rightarrow t\bar{t}$  process contributes 80-90% to the total top pair cross section in the LHC centre-of-mass  
 159 energy regime of 7-14 TeV [4]. In [Table 1.5](#) the predicted top pair production cross sections are  
 given for the LHC and Tevatron.

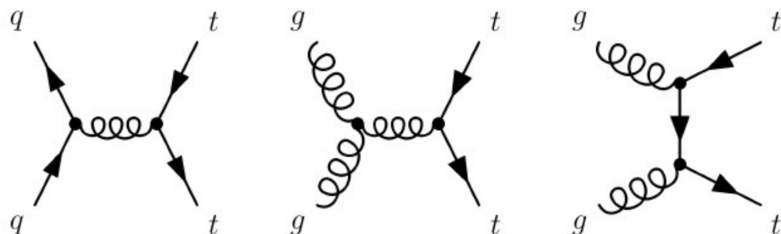


**Figure 1.1:** Leading order diagrams of the top pair production. Gluon fusion (right and middle) are the dominant processes at the LHC, while quark fusion (left) is the dominant one at Tevatron.

160

161 The singly produced top quarks are produced via the electroweak interaction. These production  
 162 mechanisms are subdivided at leading order into three main channels based on the virtuality  
 163 ( $Q^2 = -p_\mu p^\mu$ ) of the exchanged W boson. In [Figure 1.2](#), the corresponding Feynman diagrams  
 164 are shown. The single top quark production cross section, given in [Table 1.6](#), are smaller than

**Table 1.5:** Predictions on the top quark pair production cross sections at next-to-next-to-leading order with next-to-next-to-leading log soft gluon resummation per centre-of-mass energy [4]. The first uncertainty is from scale dependence, while the second uncertainty originates from parton density functions.

Experiment	Top mass	Centre-of-mass energy	Cross section (pb)
Tevatron	$m_t = 173.3 \text{ GeV}$	$\sqrt{s} = 1.96 \text{ TeV}$	$\sigma_{\bar{t}\bar{t}} = 7.16^{+0.11+0.17}_{-0.20-0.12}$
LHC	$m_t = 173.2 \text{ GeV}$	$\sqrt{s} = 7 \text{ TeV}$	$\sigma_{\bar{t}\bar{t}} = 173.6^{+4.5+8.9}_{-5.9-8.9}$
LHC	$m_t = 173.2 \text{ GeV}$	$\sqrt{s} = 8 \text{ TeV}$	$\sigma_{\bar{t}\bar{t}} = 247.7^{+6.3+11.5}_{-8.5-11.5}$
LHC	$m_t = 173.2 \text{ GeV}$	$\sqrt{s} = 13 \text{ TeV}$	$\sigma_{\bar{t}\bar{t}} = 816.0^{+19.4+34.4}_{-28.6-34.4}$

165 the top pair production cross sections since the electroweak coupling strength is smaller than  
 166 the strong coupling strength. In addition, for the single top production, there the need of sea  
 167 quarks ( $b, \bar{q}$ ) in the initial states for which the parton density functions increase less steeply at  
 low momentum fractions compared to the gluon parton density functions.

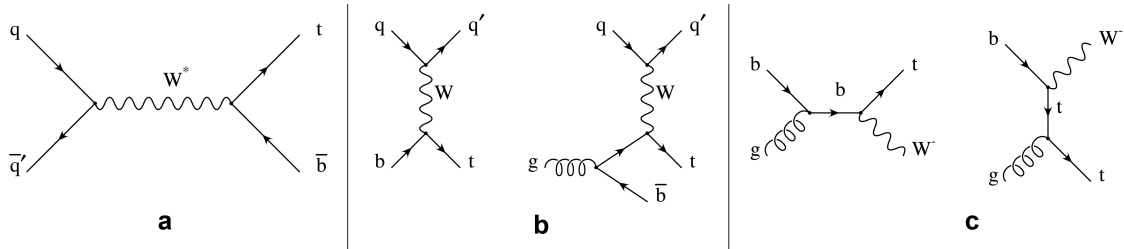


**Figure 1.2:** Leading order Feynman diagrams of the electroweak production of single top quarks in the  $s$ -channel (left),  $t$ -channel (middle), and for the  $tW$  associated production. Figure taken from [singletop].

168

169 The production via the  $t$ -channel has a virtuality of the  $W$  boson  $Q^2 > 0$ , making it space-like.  
 170 It is produced via the scattering of the  $W$  boson of a bottom quark coming from a proton or  
 171 from gluon splitting ( $g \rightarrow b\bar{b}$ ). This process is also known as  $W$ -gluon fusion production. It has  
 172 the highest single top quark cross section in proton collisions and the top quark production is  
 173 roughly twice more than the antitop quarks. This is a consequence of the up-down valence  
 174 quark composition of the proton. This feature makes the  $t$ -channel sensitive to the parton  
 175 density functions of the proton. The  $s$ -channel is the production mechanism with the smallest  
 176 cross section. Here the  $W$  boson is time-like ( $Q^2 < 0$ ) which requires the  $W$  boson to have a  
 177 large virtuality to produce the heavier top quark. It is produced from two quarks belonging  
 178 to the same isodoublet (e.g.  $u \bar{d}$ ) and subsequently decays to  $t \bar{b}$ . This process get enhanced  
 179 by many beyond the Standard Model scenarios via the addition of new heavy particles such  
 180 as  $W'$ . The  $tW$ -channel has a top quark produced in association with a  $W$  boson produced on  
 181 shell  $Q^2 = -m_W^2$ . This mode is negligible at Tevatron, but of relevant size at the LHC. The  
 182  $tW$ -channel is sensitive to new physics affecting the  $Wtb$  vertex.

**Table 1.6:** Predictions on the single top quark production cross sections at next-to-next-to-leading order per centre-of-mass energy [4]. The uncertainties from scale dependence and from parton density functions are combined in quadrature. For the  $t$ -channel the relative proportions to  $t$  and  $\bar{t}$  are 65% and 35%. For the  $s$ -channel this respectively 69% and 31%. The  $tW$ -channel has an equal proportion of top and antitop quarks.

Experiment	Centre-of-mass energy	Cross section (pb)		
		$t$ -channel	$s$ -channel	$tW$ -channel
Tevatron	$\sqrt{s} = 1.96 \text{ TeV}$	$\sigma_{t+\bar{t}} = 2.06^{+0.13}_{-0.13}$	$\sigma_{t+\bar{t}} = 1.03^{+0.05}_{-0.05}$	-
LHC	$\sqrt{s} = 7 \text{ TeV}$	$\sigma_{t+\bar{t}} = 65.7^{+1.9}_{-1.9}$	$\sigma_{t+\bar{t}} = 1.03^{+0.05}_{-0.05}$	-
LHC	$\sqrt{s} = 8 \text{ TeV}$	$\sigma_{t+\bar{t}} = 85.1^{+2.5}_{-1.4}$	$\sigma_{t+\bar{t}} = 1.03^{+0.05}_{-0.05}$	-
LHC	$\sqrt{s} = 13 \text{ TeV}$	$\sigma_{t+\bar{t}} = 2.06^{+0.13}_{-0.13}$	$\sigma_{t+\bar{t}} = 1.03^{+0.05}_{-0.05}$	-

### 183 Experimental results on the SM top quark

## 184 1.5 Motivations for new physics

185 Many high energy experiments confirm the success of the SM. In particular the scalar boson,  
 186 the cornerstone of the SM, has consecrated the theory. Unfortunately there are also strong  
 187 indications that the SM ought to be a lower energy expression of a more global theory. The  
 188 existence of physics beyond the SM (BSM) [15] is strongly motivated. These motivations are  
 189 based on direct evidence from observation such as the existence of neutrino masses, the existence  
 190 of dark matter and dark energy, or the matter-antimatter asymmetry, and also from theoretical  
 191 problems such as the hierarchy problem, the coupling unification or the large numbers of free  
 192 parameters in the SM.

193 In the SM, the neutrino is assumed to be massless, whilst experiments with solar, atmospheric,  
 194 reactor and accelerator neutrinos have established that neutrinos can oscillate and change  
 195 flavour during flight [16, 17]. These oscillations are only possible when neutrino's have masses.  
 196 The flavour neutrinos ( $\nu_e$ ,  $\nu_\mu$ ,  $\nu_\tau$ ) are then linear expressions of the fields of at least three mass  
 197 eigenstate neutrinos  $\nu_1$ ,  $\nu_2$ , and  $\nu_3$ .

198 The ordinary or baryonic matter described by the SM describes only 5% of the mass (energy)  
 199 content of the universe. Astrophysical evidence indicated that dark matter is contributing  
 200 to approximately 27%, and dark energy to 68% of the content of the universe. From the  
 201 measurements of the temperature and polarizations anisotropies of the cosmic microwave  
 202 background by the Planck experiment [18], the density of cold non baryonic matter is determined.  
 203 Cold dark matter is assumed to be only sensitive to the weak and gravitational force, leading  
 204 to only one possible SM candidate: the neutrino. However, these are too light to account for  
 205 the vast amount of dark matter and other models are needed. Dark energy is assumed to be  
 206 responsible for the acceleration in the expansion of the universe [19].

207 At the Big Bang matter and antimatter is assumed to be produced in equal quantities. However,  
 208 it is clear that we are surrounded by matter. So where did all the antimatter go? In 1967,  
 209 Sakharov identified three mechanisms that are necessary to obtain a global matter antimatter  
 210 asymmetry [20]. These mechanisms are those of baryon and lepton number violation, that at a

given moment in time there was a thermal imbalance for the interactions in the universe, and  
there is charge C and charge parity CP violation<sup>3</sup>.

The large numbers of free parameters in the SM are taken as nine fermion masses, three CKM mixing angles and one CP violating phase, one EM coupling constant  $g'$ , one weak coupling constant  $g$ , one strong coupling constant  $g_s$ , one QCD vacuum angle, one vacuum expectation value, and one mass of the scalar boson. This large number of free parameters lead to the expectation of a more elegant, general theory beyond the SM.

The hierarchy problem [21] is related to the huge difference in energy between the weak scale and the Planck scale. The vev of the Brout-Englert-Higgs field determines the weak scale that is approximately 246 GeV. The radiative corrections to the scalar boson squared mass  $m_H^2$ , coming from its self couplings and couplings to fermions and gauge bosons, are quadratically proportional to the ultraviolet momentum cut-off  $\Lambda_{UV}$ . This cut-off is at least equal to the energy to which the SM is valid without the need of new physics. The SM is valid up to the Planck mass making the correction to  $m_H^2$  about thirty orders of magnitude larger than  $m_H^2$ . This implies that an extraordinary cancellation of terms should happen. This is also known as the naturalness problem of the H boson mass.

The correction to the squared mass of the scalar boson coming from a fermion  $f$ , coupling to the scalar field  $\phi$  with a coupling  $\lambda_f$  is given by

$$\Delta m_H^2 = -\frac{|\lambda_f|^2}{8\pi^2} \Lambda_{UV}^2, \quad (1.18)$$

while the correction to the mass from a scalar particle  $S$  with a mass  $m_S$ , coupling to the scalar field with a Lagrangian term  $-\lambda_{mathrms} |\phi|^2 |S|^2$  is

$$\Delta m_H^2 = -\frac{|\lambda_S|^2}{16\pi^2} \left( \Lambda_{UV}^2 - 2m_S^2 \ln \left( \frac{\Lambda_{UV}}{m_S} \right) + \dots \right). \quad (1.19)$$

As one can see the correction term to  $m_H^2$  is much larger than  $m_H^2$  itself. By introducing BSM physic models that introduce new scalar particles at TeV scale that couple to the scalar boson can cancel the  $\Lambda_{UV}^2$  divergence and avoid this fine-tuning.

The choice of the  $SU_C(3) \times SU_L(2) \times U_Y(1)$  symmetry group itself as well as the separate treatment of the three forces included in the SM raises concern. The intensity of the forces show a large disparity around the electroweak scale, but have comparable strengths at higher energies. The electromagnetic and weak forces are unified in a electroweak interaction, but the strong coupling constant does not encounter the other coupling constants at high energies. In order to reach a grand unification, the running of couplings can be modified by the addition of new particles in BSM models.

---

<sup>3</sup>The rate of a process  $i \rightarrow f$  can be different from the CP-conjugate process:  $\tilde{i} \rightarrow \tilde{f}$ . The SM includes sources of CP-violation through the residual phase of the CKM matrix. However, these could not account for the magnitude of the asymmetry observed.

237 **1.6 An effective approach beyond the SM: FCNC involving a top**  
 238 **quark**

239 The closeness of the top mass to the electroweak scale led physicist to believe that it is a sensitive  
 240 probe for new physics. Its property study is therefore an important topic of the experimental  
 241 program at the LHC. Several extensions of the SM enhance the FCNC branching ratios and can  
 242 be probed at the LHC [14], from which some of them are shown in Table 1.7. Previous searches  
 243 have been performed at the Fermilab Tevatron by the CDF [22] and D0 [23] collaborations,  
 and at the LHC by the ATLAS [24–27] and CMS [28–32] collaborations.

**Table 1.7:** The predicted branching ratios  $\mathcal{B}$  for FCNC interactions involving the top quark in some BSM models [14]: quark singlet (QS), generic two Higgs doublet model (2HDM) and the minimal supersymmetric extensions to the SM (MSSM);

Process	QS	2HDM	MSSM	Process	QS	2HDM	MSSM
$t \rightarrow uZ$	$\leq 1.1 \cdot 10^{-4}$	—	$\leq 2 \cdot 10^{-6}$	$t \rightarrow cZ$	$\leq 1.1 \cdot 10^{-4}$	$\leq 10^{-7}$	$\leq 2 \cdot 10^{-6}$
$t \rightarrow u\gamma$	$\leq 7.5 \cdot 10^{-9}$	—	$\leq 2 \cdot 10^{-6}$	$t \rightarrow c\gamma$	$\leq 7.5 \cdot 10^{-9}$	$\leq 10^{-6}$	$\leq 2 \cdot 10^{-6}$
$t \rightarrow ug$	$\leq 1.5 \cdot 10^{-7}$	—	$\leq 8 \cdot 10^{-5}$	$t \rightarrow cg$	$\leq 1.5 \cdot 10^{-7}$	$\leq 10^{-4}$	$\leq 8 \cdot 10^{-5}$
$t \rightarrow uH$	$\leq 4.1 \cdot 10^{-5}$	$\leq 5.5 \cdot 10^{-6}$	$\leq 10^{-5}$	$t \rightarrow cH$	$\leq 4.1 \cdot 10^{-5}$	$\leq 10^{-3}$	$\leq 10^{-5}$

244

245 The impact of BSM models can be written in a model independent way by means of an effective  
 246 field theory valid up to an energy scale  $\Lambda$ . The leading effects are parametrized by a set of  
 247 fully gauge symmetric dimension-6 operators that are added to the SM Lagrangian and can be  
 248 reduced to a minimal set of operators as discussed in [33, 34]. The full Lagrangian, neglecting  
 249 neutrino physics, in the fully gauge symmetric case is given by

$$\mathcal{L}_{\text{SM+EFT}} = \mathcal{L}_{\text{SM}} + \sum_i \frac{\bar{c}_i}{\Lambda^2} \mathcal{O}_i + \mathcal{O}\left(\frac{1}{\Lambda^3}\right), \quad (1.20)$$

where the Wilson coefficients  $\bar{c}_i$  depend on the considered theory and on the way that new physics couples to the SM particles. Considering that  $\Lambda$  is large, contributions suppressed by powers of  $\Lambda$  greater than two are neglected. Moreover, all four fermion operators are omitted for the rest of this thesis. After electroweak symmetry breaking the operators induce [14, 35] both corrections to the SM couplings and new interactions at tree level such as FCNC interactions. The FCNC interactions of the top quark that are not present in the SM are given by

$$\mathcal{L}_{\text{EFT}}^t = \frac{\sqrt{2}}{2} \sum_{q=u,c} \left[ g' \frac{\kappa_{t\gamma q}}{\Lambda} A_{\mu\nu} \bar{t} \sigma^{\mu\nu} (f_{\gamma q}^L P_L + f_{\gamma q}^R P_R) q \right. \quad (1.21)$$

$$+ \frac{g}{2\cos\theta_W} \frac{\kappa_{tZq}}{\Lambda} Z_{\mu\nu} \bar{t} \sigma^{\mu\nu} (f_{Zq}^L P_L + f_{Zq}^R P_R) q \quad (1.22)$$

$$+ \frac{\sqrt{2}g}{4\cos\theta_W} \zeta_{tZq} \bar{t} \gamma^\mu (\tilde{f}_q^L P_L + \tilde{f}_q^R P_R) q Z_\mu \quad (1.23)$$

$$+ g_S \frac{\kappa_{gqt}}{\Lambda} Z_{\mu\nu} \bar{t} \sigma^{\mu\nu} (f_{gq}^L P_L + f_{gq}^R P_R) q G_{\mu\nu}^a \quad (1.24)$$

$$+ \eta_{Hqt} \bar{t} (\hat{f}_q^L P_L + \hat{f}_q^R P_R) q H + \text{h.c.} \right], \quad (1.25)$$

where the the value of the FCNC couplings at scale  $\Lambda$  are represented by  $\kappa_{tZq}, \kappa_{gqt}, \kappa_{t\gamma q}, \zeta_{tZq}$ , and  $\eta_{Hqt}$ . These are assumed to be real and positive, with the unit of  $\text{GeV}^{-1}$  for  $\kappa_{txq}/\Lambda$  and no unit for  $\zeta_{xqt}$  and  $\eta_{xqt}$ . In the equation  $\sigma^{\mu\nu}$  equals to  $\frac{i}{2} [\gamma^\mu, \gamma^\nu]$ , and the left- and right-handed chirality projector operators are denoted by  $P_L$  and  $P_R$ . The electromagnetic coupling constant is denoted by  $g'$ , the strong interaction coupling is denoted as  $g_s$ , while the electroweak interaction is parametrised by the coupling constant  $g$  and the electroweak mixing angle  $\theta_W$ . The complex chiral parameters are normalized according to  $|f_{xq}^L|^2 + |f_{xq}^R|^2 = 1$ ,  $|\tilde{f}_q^L|^2 + |\tilde{f}_q^R|^2 = 1$ , and  $|\hat{f}_q^L|^2 + |\hat{f}_q^R|^2 = 1$ . In the expression for  $\mathcal{L}_{\text{EFT}}^t$ , the unitary gauge is adopted and the scalar field is expanded around its vacuum expectation value with  $H$  being the SM scalar boson, and the field strength tensors of the photon  $A_\mu$ , the gluon field  $G_\mu^{1\dots 8}$ , and the Z boson  $Z_\mu^0$  are defined as

$$A_{\mu\nu} = \partial_\mu A_\nu - \partial_\nu A_\mu, \quad Z_{\mu\nu} = \partial_\mu Z_\nu - \partial_\nu Z_\mu, \quad \text{and} \quad G_{\mu\nu} = \partial_\mu G_\nu^a - \partial_\nu G_\mu^a + g_S f_{bc}^a G_\mu^b G_\nu^c. \quad (1.26)$$

- 250 Denoting the structure constant of the  $SU_C(3)$  group as  $f_{bc}^a$ . Note that there are two coupling  
 251 constants arising in  $\mathcal{L}_{\text{EFT}}^t$ , which is a residue of electroweak symmetry breaking. The massive Z  
 252 boson will appear in both the  $Z_\mu^0$  field as well as the covariant derivative , leading to an extra  
 253 Z-vertex.  
 254

**NOTE:**  
should I  
explain cov.  
der?

## 1.7 Experimental constraints on top-FCNC

Experiments commonly put limits on the branching ratio's which allow an easier interpretation across different EFT models by use of the branching ratio  $\mathcal{B}$

$$\mathcal{B}(t \rightarrow qX) = \frac{\delta_{txq}^2 \Gamma_{t \rightarrow qX}}{\Gamma_t}, \quad (1.27)$$

- 255 where  $\Gamma_{t \rightarrow qX}$  represents the FCNC decay width<sup>4</sup> for a coupling strength  $\delta_{txq}^2 = 1$ , and  $\Gamma_t$  the full  
 256 decay width of the top quark. In the SM, supposing a top quark mass of 172.5 GeV, the full  
 257 width becomes  $\Gamma_t^{\text{SM}} = 1.32 \text{ GeV}$  [36].

- 258 Searches for top-FCNC usually adopt a search strategy depending on the experimental set-up  
 259 and the FCNC interaction of interest, looking either for FCNC interactions in the production of  
 260 a single top quark or in its decay for top pair interactions. In Figure 1.3, these two cases are  
 261 shown for the tZq vertex.  
 262

- 263 The observation of top-FCNC interactions has yet to come and experiments have so far only  
 264 been able to put upper bounds on the branching ratios. An overview of the best current limits is  
 265 given in Table 1.8 . In Figure 1.4 a comparison is shown between the current best limits set by  
 266 ATLAS and CMS with respect to several BSM model benchmark predictions. From there one can  
 267 see that FCNC searches involving a Z or H boson are close to excluding or confirming several  
 268 BSM theories.

**NOTE:**  
Check at-  
las result  
for tZq from  
top2017  
proceedings  
when they  
appear

---

<sup>4</sup>The decay width of a certain process represents the probability per unit time that a particle will decay. The total decay width, defined as all possible decay widths of a particle, is inversely proportional to its lifetime.



**Figure 1.3:** Feynman diagrams for the  $tZq$  FCNC interaction, where the FCNC interaction is indicated with the shaded dot. (a) Single top production through an FCNC interaction. (b) Top pair production with an FCNC induced decay.

**Table 1.8:** Overview of the most stringent observed and expected experimental limits on top-FCNC branching ratios  $\mathcal{B}$  at 95% confidence level.

Process	Search mode	Observed $\mathcal{B}$	Expected $\mathcal{B}$	Experiment
$t \rightarrow uZ$	top pair decay and single top production	$2.2 \cdot 10^{-4}$	$2.7 \cdot 10^{-4}$	CMS [28]
$t \rightarrow u\gamma$	single top production	$1.3 \cdot 10^{-4}$	$1.9 \cdot 10^{-4}$	CMS [30]
$t \rightarrow ug$	single top production	$4.0 \cdot 10^{-5}$	$3.5 \cdot 10^{-5}$	ATLAS [25]
$t \rightarrow uH$	top pair decay	$2.4 \cdot 10^{-3}$	$1.7 \cdot 10^{-3}$	ATLAS [27]
$t \rightarrow cZ$	top pair decay and single top production	$4.9 \cdot 10^{-4}$	$12 \cdot 10^{-4}$	CMS [28]
$t \rightarrow c\gamma$	single top production	$2.0 \cdot 10^{-3}$	$1.7 \cdot 10^{-3}$	CMS [30]
$t \rightarrow cg$	single top production	$2.0 \cdot 10^{-4}$	$1.8 \cdot 10^{-4}$	ATLAS [25]
$t \rightarrow cH$	top pair decay	$2.2 \cdot 10^{-3}$	$1.6 \cdot 10^{-3}$	CMS [27]

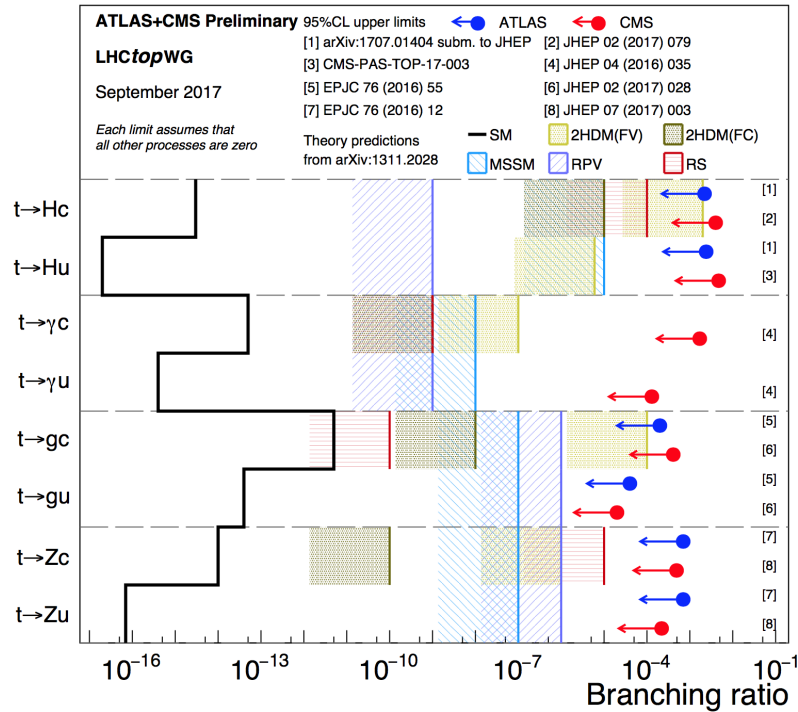


**Figure 1.4:** Current best limits set by CMS and ATLAS for top-FCNC interactions.



# Experimental set-up

# 2

---

270 The main objective of the Large Hadron Collider (LHC) was the search for the Brout-Englert-  
 271 Higgs boson. The Large Electron Positron (LEP) [37] and Tevatron [38] experiments had  
 272 established that the mass of the scalar boson has to be larger than 114 GeV [39, 40], and smaller  
 273 than approximate 1 TeV due to unitarity and perturbativity constraints [41]. On top of this,  
 274 the search for new physics such as supersymmetry or the understanding of dark matter were  
 275 part of the motivation for building the LHC. Since the start of its operation, the LHC is pushing  
 276 the boundaries of the Standard Model, putting the most stringent limits on physics beyond the  
 277 Standard Model as well as precision measurements of the parameters of the Standard Model. A  
 278 milestone of the LHC is the discovery the scalar boson in 2012 by the two largest experiments  
 279 at the LHC [7, 8].

280 This chapter is dedicated to the experimental set up of the LHC and the Compact Muon  
 281 Solenoid (CMS) experiment. [Section 2.1](#) describes the LHC and its acceleration process for  
 282 protons to reach their design energies. The CMS experiment and its components are presented  
 283 in [Section 2.2](#).

## 284 2.1 The Large Hadron Collider

285 The LHC has started its era of cutting edge science on 10 September 2008 [42] after approval by  
 286 the European Organisation of Nuclear Research (CERN) in 1995 [43]. Installed in the previous  
 287 LEP tunnels, the LHC consists of a 26.7 km ring, that is installed between 45 and 170 m under  
 288 the French-Swiss border amidst Cessy (France) and Meyrin (Switzerland). Built to study rare  
 289 physics phenomena at high energies, the LHC can accelerate two type of particles, protons or  
 290 ions  $Pb^{45+}$ , and provides collisions at four interaction points, where the particle bunches are  
 291 crossing. Experiments for studying the collisions are installed on each interaction point.

292 As can be seen in [Figure 2.1](#), the LHC is last element in a chain that creates, injects and  
 293 accelerates protons. The starting point is the ionisation of hydrogen, creating protons that are  
 294 injected in a linear accelerator (LINAC 2). Here, the protons obtain an energy of 50 MeV. They  
 295 continue to the proton synchrotron booster (PSB or Booster), where the packs of protons are  
 296 accelerated to 1.4 GeV and each pack is split up in twelve bunches with 25 ns spacing for Run 2  
 297 (50 ns for Run 1). The proton synchrotron (PS) then increases their energy to 25 GeV before the

super proton synchrotron (SPS) increases the proton energy up to 450 GeV. Each accelerator ring expands in radius in order to reduce the energy loss of the protons by synchrotron radiation<sup>1</sup>. Furthermore, the magnets responsible for the bending of the proton trajectories have to be strong enough to sustain to higher proton energy. Ultimately, the protons are injected into opposite directions into the LHC, where they are accelerated to 3.5 TeV (in 2010 and 2011), 4 TeV (in 2012 and 2013) or 6.5 TeV (in 2015 and 2016) [44]. Before the start of the LHC in 2010, the previous energy record was held by the Tevatron collider at Fermilab, colliding proton with antiprotons at  $\sqrt{s} = 1.96$  TeV. When completely filled, the LHC nominally contains 2220 bunches in Run 2, compared to 1380 in Run 1 (design: 2200).

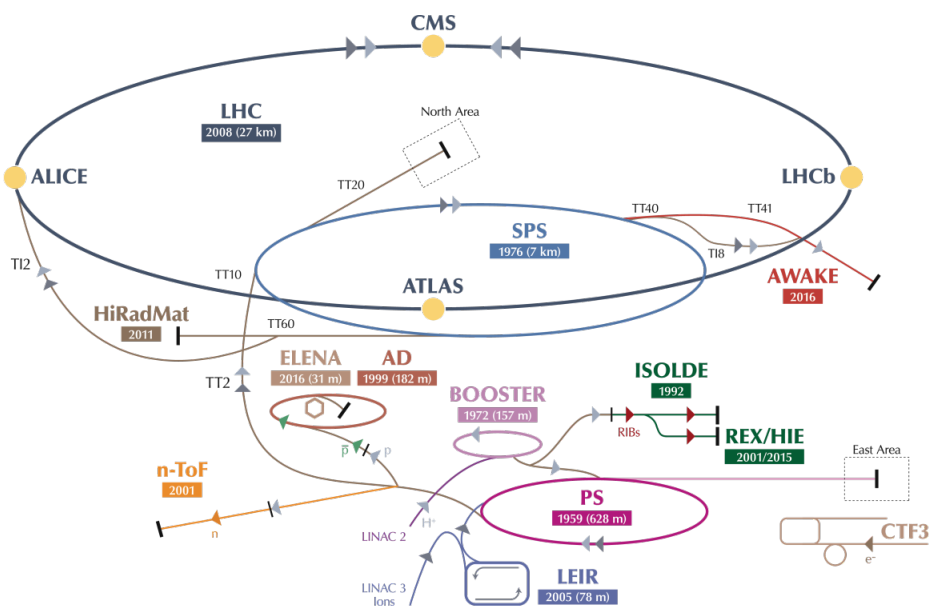


**Figure 2.1:** Schematic representation of the accelerator complex at CERN [45]. The LHC (dark blue) is the last element in chain of accelerators. Protons are successively accelerated by LINAC 2, the Booster, the Proton Synchrotron (PS) and the Super Proton Synchrotron (SPS) before entering the LHC.

306

Inside the LHC ring [46], the protons are accelerated by the means of radio frequency cavities, while 1232 dipole magnets of approximately 15 m long, each weighing 35 t ensure the deflection of the beams. The two proton beams circulate in opposite direction in separate pipes inside of the magnet. Through the use of a strong electric current in the coils around the beam pipe, magnetic fields are generated and cause the protons to bend in the required orbits. In order to get the coil to become superconducting and able to produce - with the aid of an iron return yoke - a strong magnetic field of 8.3 T, the magnet structure is surrounded by a vessel. This vessel is filled with liquid Helium making it possible to cool down the magnet to 1.9 K. In order to get more focussed and stabilised proton beams, additional higher-order multipole and corrector magnets are placed along the LHC beam line.

<sup>1</sup>This energy loss is proportional to the fourth power of the proton energy and inversely proportional to the bending radius.

317     The LHC is home to seven experiments, each located on an interaction point:

- 318     • A Toroidal LHC ApparatuS (ATLAS) [47] and the Compact Muon Solenoid (CMS) [48]  
 319       experiments are the two general purpose detectors at the LHC. They both have a hermetic,  
 320       cylindrical structure and were designed to search for new physics phenomena along with  
 321       precision measurements of the Standard Model. The existence of two distinct experiments  
 322       allows cross-confirmation of any discovery.
- 323     • A Large Ion Collider Experiment (ALICE) [49] and the LHC Beauty (LHCb) [50] exper-  
 324       iments are focusing on specific phenomena. ALICE studies strongly interacting matter  
 325       at extreme energy densities where a quark-gluon plasma forms in heavy ion collisions  
 326       (Pb-Pb or p-Pb). LHCb searches for differences between matter and antimatter with the  
 327       focus on b physics..
- 328     • The forward LHC (LHCf) [51] and the TOTal cross section, Elastic scattering and diffraction  
 329       dissociation Measurement (TOTEM) [52] experiments are two smaller experiments that  
 330       focus on head on collisions. LHCf consists of two parts placed before and after ATLAS  
 331       and studies particles created at very small angles. TOTEM is placed in the same cavern as  
 332       CMS and measures the total proton-proton cross section and studies elastic and diffractive  
 333       scattering.
- 334     • The Monopoles and Exotics Detector At the LHC (MoEDAL) [53] experiment is situated  
 335       near LHCb and tries to find magnetic monopoles.

For the enhancement of the exploration of rare events and thus enhancing the number of collisions, high beam energies as well as high beam intensities are required. The luminosity [54] is a measurement of the number of collisions that can be produced in a detector per square meter and per second and is the key role player in this enhancement. The LHC collisions create a number of events per second given by

$$N_{\text{event}} = L\sigma_{\text{event}}, \quad (2.1)$$

where  $\sigma_{\text{event}}$  is the cross section of the event of interest and  $L$  the machine luminosity. This luminosity depends only on the beam parameters and is for a Gaussian beam expressed as

$$L = \frac{1}{4\pi} N_b n_b f_{\text{rev}} \frac{N_b}{\epsilon_n} \left( 1 + \left( \frac{\theta_c \sigma_z}{2\sigma^*} \right)^2 \right)^{-\frac{1}{2}} \frac{\gamma_r}{\beta^*}. \quad (2.2)$$

- 336     The number of particles per bunch is expressed by  $N_b$ , while  $n_b$  is the number of bunches  
 337       per beam,  $f_{\text{rev}}$  the revolution frequency,  $\gamma_r$  the relativistic gamma factor,  $\epsilon_n$  the normalized  
 338       transverse beam emittance - a quality for the confinement of the beam ,  $\beta^*$  the beta function at  
 339       the collision point - a measurement for the width of the beam,  $\theta_c$  the angle between two beams  
 340       at the interaction point,  $\sigma_z$  the mean length of one bunch, and  $\sigma^*$  the mean height of one bunch.  
 341     In Equation 2.2, the blue part represents the stream of particles, the red part the brilliance, and  
 342       the green part the geometric reduction factor due to the crossing angle at the interaction point.

343 The peak design luminosity for the LHC reached in 2016 is  $10^{34} \text{ m}^{-2}\text{s}^{-1}$ , which leads to about  
 344 1 billion proton interactions per second. In 2016, the LHC was around 10% above this design  
 345 luminosity [55]. The luminosity is not a constant in time since it diminishes due to collisions  
 346 between the beams, and the interaction of the protons and the particle gas that is trapped in  
 347 the centre of the vacuum tubes due to the magnetic field. The diffusion of the beam degrades  
 348 the emittance and therefore also the luminosity. For this reason, the mean lifetime of a beam  
 349 inside the LHC is around 15 h. The integrated luminosity - the luminosity provided in a certain  
 350 time range - recorded by CMS and ATLAS over the year 2016 is given in Figure 2.2. In Run 2,  
 the peak luminosity is  $13\text{-}17 \cdot 10^{33} \text{ cm}^{-2}\text{s}^{-1}$  compared to  $7.7 \cdot 10^{33} \text{ cm}^{-2}\text{s}^{-1}$  in Run 1.

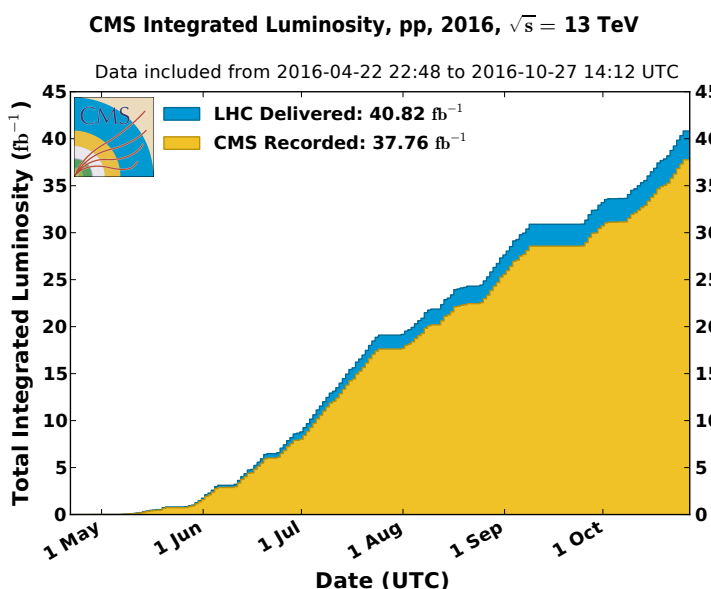


**Figure 2.2:** Cumulative offline luminosity measured versus day delivered to (blue), and recorded by CMS (orange) during stable beams and for proton collisions at 13 TeV centre-of-mass energy in 2016. The delivered luminosity accounts for the luminosity delivered from the start of stable beams until the LHC requests CMS to turn off the sensitive detectors to allow a beam dump or beam studies.

351

352 Multiple proton-proton interactions can occur during one bunch crossing, referred to as  
 353 pileup. On average, the number of pileup events is proportional to the luminosity times the total  
 354 inelastic proton-proton cross section. In 2016, an average of about 27 of pileup interactions  
 355 has been observed in 13 TeV proton collisions at the interaction point of CMS. For 2012, this  
 356 number was about 21 pileup interactions for 8 TeV collisions.

## 357 2.2 The Compact Muon Solenoid

358 At one of the collision points of the LHC, the CMS detector[56–58] is placed. Weighing 14 000  
 359 t, This cylindrical detector is about 28.7 m long and 15 m in diameter, weighing around 14 000  
 360 t. It has an onion like structure of several specialised detectors and contains a superconducting  
 361 solenoid with a magnetic field of 3.8 T. The CMS detector is designed in a way that it can  
 362 address the needs of physics coming from the LHC. Living in a hadronic environment, multi-jet

processes produced by the strong interaction are a main source of background for rare physics processes. Therefore, good identification, momentum resolution, and charge determination of muon, electrons and photons is one of the main goals of the CMS detector. Further it provides a good charged particle momentum resolution and reconstruction efficiency in the inner tracker such that for example jets coming from b quarks or tau particles can be identified. Also the electromagnetic resolution for an efficient photon and lepton isolation as well as a good hadronic calorimeter for the missing transverse energy were kept into account while designing CMS. In [Figure 2.3](#), an overview of the CMS detector is given.

The LHC provides many collisions in a short amount of time. In order to discriminate between consecutive collisions - known as out of time pile up events - , CMS has to complete the full data acquisition for one collision event before the next one happens (around 25 ns in Run II and around 50 ns in Run I [59]). Furthermore, since the photons are in packets, around 21 in Run I and approximately 40 in Run II inelastic collisions happen every beam crossing . This creates a great amount of background processes in the detector called in time pile up events. Due to this difficult conditions, the detector has a high granularity which on its turn creates a need for huge number of synchronized electronic channels. Furthermore, due to high flux of particles in the regions close to the beam, the electronics have to be able to endure high radiation.

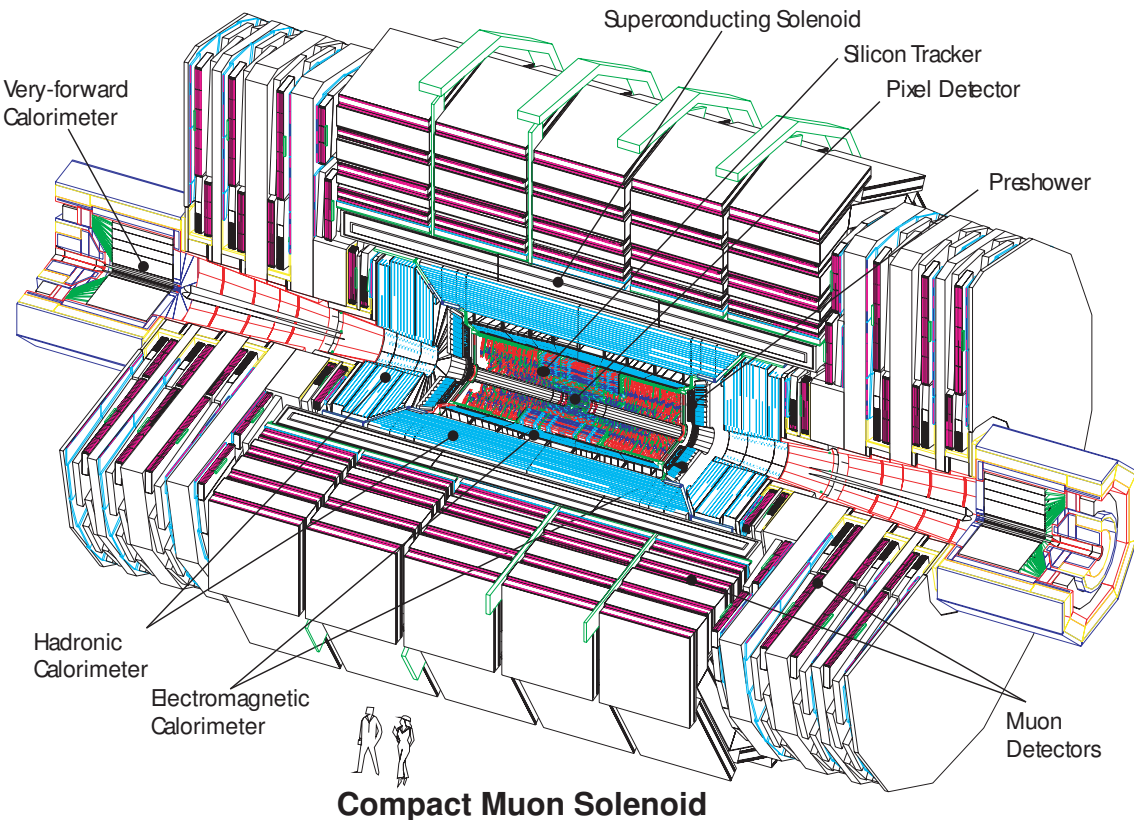


[Figure 2.3](#): Mechanical layout of the CMS detector[60].

Before the start of taking collision data for 13 TeV operations on 3 June, CMS had a long shutdown (LS1)[61]. During this shut down several upgrades were performed. The innermost

part of detection material in CMS (pixel) is made of three concentric cylindrical layers in run I. At the end of 2016 it is upgraded by adding a fourth layer, enhancing the particle tracking capabilities of CMS. In order to be able to incorporate this new layer, the section of the beryllium beam pipe within CMS was replaced by a narrower one during LS1. For this, the pixel was removed and reinserted into CMS. In order to avoid long damage caused by the intense particle flux at the heart of CMS, the tracker is been made ready to operate at much lower temperature than before. During Run I, a small problem was detected in the electromagnetic calorimeter preshower system. For this, the preshower discs were removed, repaired and reinstalled successfully inside CMS in 2014. To help the discrimination between interesting low momentum muons coming from collisions and muons caused by backgrounds, a fourth triggering and measurement station for muons was added in each of the end caps. CMS measures the collision rate within the detector and monitors beam related backgrounds. For this, several new detectors were installed into CMS during LS1.

### 2.2.1 CMS coordinate system

The coordinate system used by CMS can be found in [Figure 2.4](#). The origin of the right handed orthogonal coordinate system is chosen to be the point of collisions. The x-axis points towards the centre of the LHC ring such that the y-axis points towards the sky, and the z-axis lies tangent to the beam axis. Since the experiment has a cylindrical shape, customary coordinates are used to describe the momentum  $\vec{p}$  : the distance  $\rho$ , the azimuthal angle  $\phi \in [-\pi, \pi]$  - the angle between the x-axis and the projection in the transverse plane of  $\vec{p}$  ( $\vec{p}_T$ ) - , the pseudo-rapidity  $\eta$  - expressed by the polar angle  $\theta$  between the direction of  $\vec{p}$  and the beam - :

$$\eta = -\ln\left(\tan\left(\frac{\theta}{2}\right)\right). \quad (2.3)$$

For the energies considered at the LHC, where  $E \gg m$ , the pseudo-rapidity is a good approximation of the rapidity  $y$

$$y = \frac{1}{2} \ln\left(\frac{E + p_z}{E - p_z}\right), \quad (2.4)$$

where the difference of rapidities of two particles is invariant under a Lorentz boost in the z-direction.

### 2.2.2 Towards the heart of CMS

The CMS detector consists of two parts; a central barrel around the beam pipe ( $|\eta| < 1.4$ ) and two plugs to ensure the hermeticity of the detector. In [Figure 2.3](#) and [Figure 2.5](#) the onion like structure of the CMS detector is visible. The choice of a solenoid of 12.9 m long and 5.9 m diameter gives the advantage of bending the particle trajectories in the transverse plane. The hadronic calorimeter, the electromagnetic calorimeter and the tracker are within the solenoid, while the muon chambers are placed outside the solenoid.

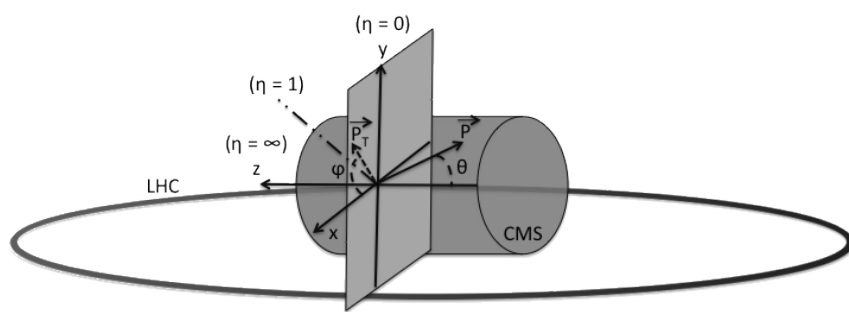


**Figure 2.4:** Representation of the coordinate system used by CMS. The point of origin is put at the collision point. The x-axis points towards the centre of the LHC ring such that the z-axis lies tangent to the beam axis.

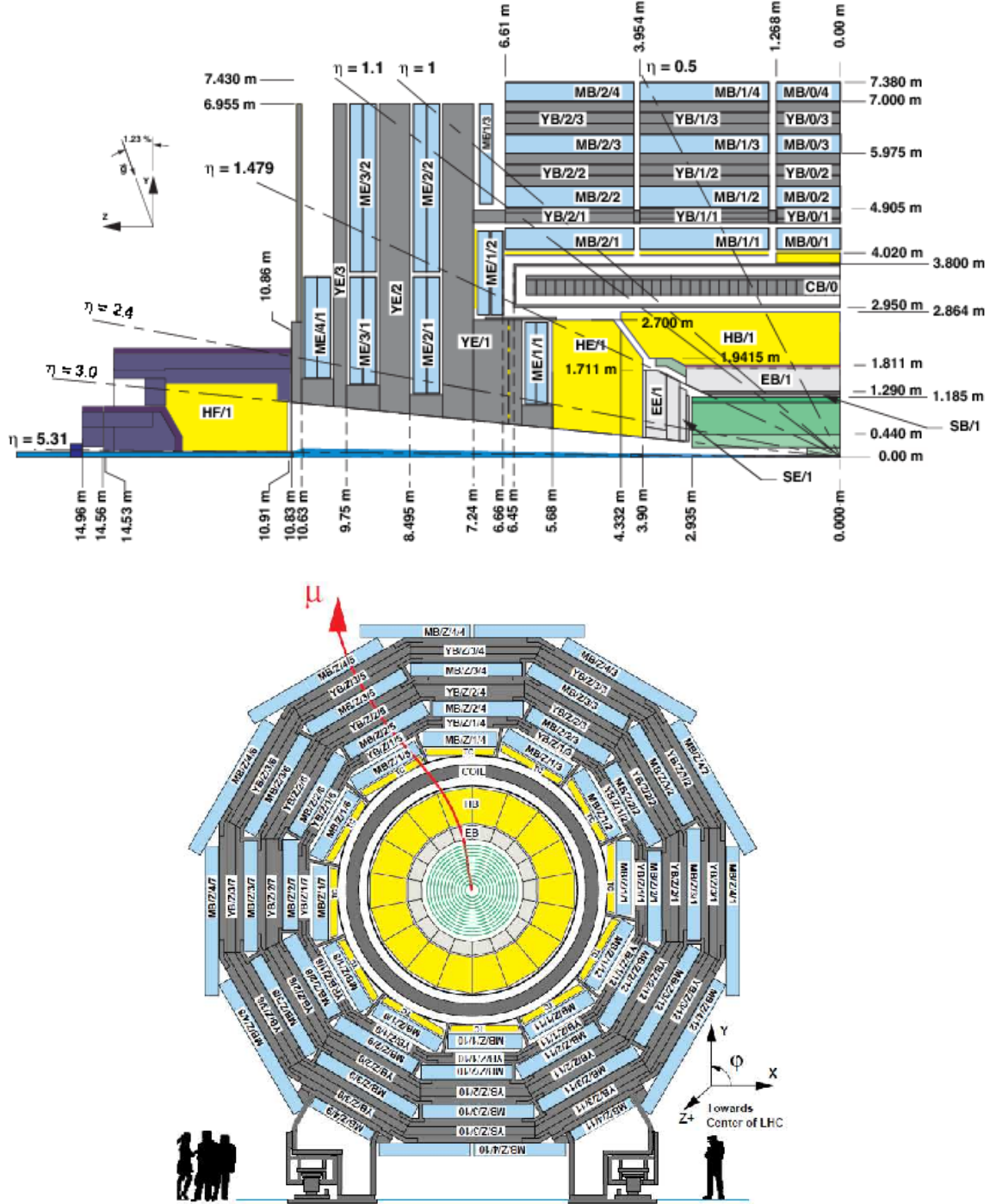


**Figure 2.5:** Schematic view of the CMS detector in the Run I configuration. (LEFT) Longitudinal view of one quarter of the detector. (RIGHT) Transversal view of one quarter of the detector. The muon system barrel elements are denoted as  $MBZ/N/S$ , where  $z = -2\dots + 2$  is the barrel wheel number,  $n = 1\dots 4$  the station number and  $S = 1\dots 12$  the sector number. Similarly, the steel return yokes are denoted as  $YBZ/N/S$ . The solenoid is denoted as  $CB0$ , while the hadronic calorimeter is denoted as  $HE$  (end cap)/ $HB$  (barrel)/ $HF$ (forward) and the electromagnetic calorimeter as  $EE$ (end cap)/ $EB$  (barrel). The green part represents the tracking system[62]

405 **2.2.2.1 Muon system**

406 The outermost part of CMS consists of the muon system. The magnet return yoke is interleaved  
 407 with gaseous detector chambers for muon identification and momentum measurement. The  
 408 barrel contains muon stations arranged in five separate iron wheels, while in the end cap four  
 409 muon stations are mounted onto three independent iron discs on each side. Each barrel wheel  
 410 has 12 sectors in the azimuthal angle.

411 The muon system is divided into three parts, shown in [Figure 2.6](#)[62]. The muon rate and  
 412 neutron induced backgrounds are small and the magnetic field is very low for the barrel, thus  
 413 CMS can use drift tube (DT) chambers. For the end caps however, the muon and background  
 414 flux is much higher and there is a need to use cathode strip chambers (CSC) which are able  
 415 to provide a faster response, higher granularity and have a better resistance against radiation.  
 416 In order to form a redundant trigger system, resistive plate chambers (RPC) are added. This  
 417 makes a total of 250 DT chambers, 540 CSC and 610 RPC. In [Figure 2.5](#) the arrangement is  
 418 shown.

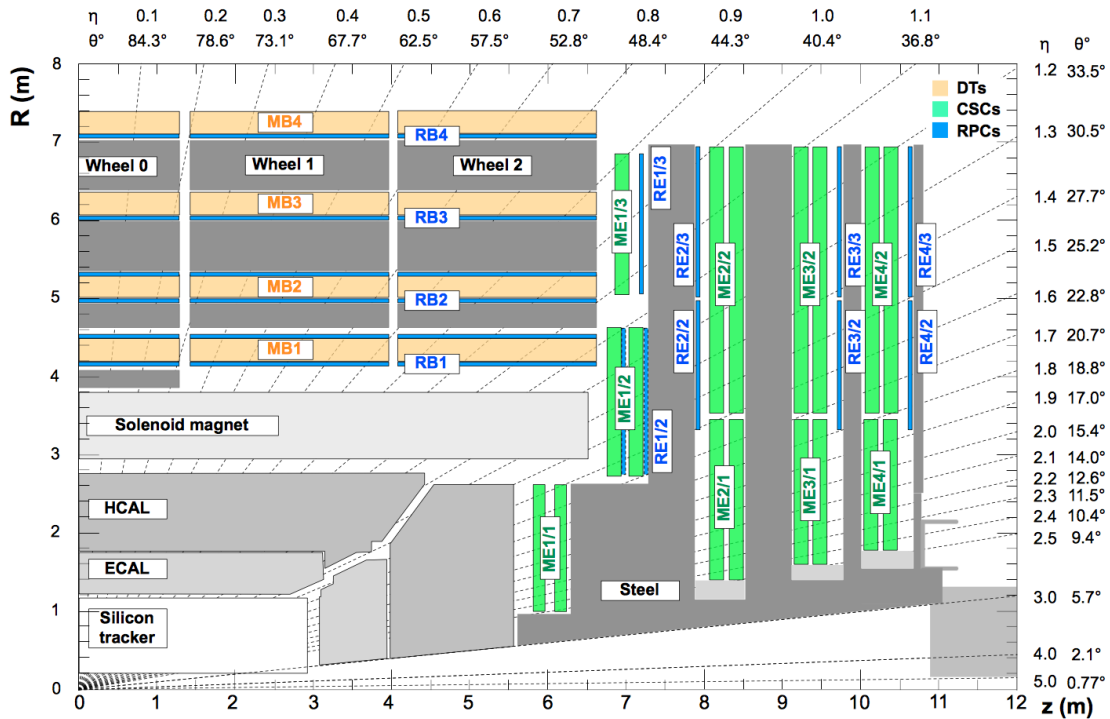


**Figure 2.6:** Schematic view of one quarter of the CMS muon system in the Run I configuration. [62]

419 Providing a measurement for  $|\eta| < 1.2$ . The DT chambers in the barrel are on average 2  
 420  $\times$  2.5 m in size and consist of 12 layers of DT cells - 4 cm wide gas tubes with positively  
 421 charged stretched wire inside - arranged in three groups of four. The  $r\phi$  coordinate is provided  
 422 by the two outside groups, while the middle group measures the  $z$  coordinate. For each  $\phi$   
 423 sector, the DT chamber is mixed with the flux return yoke. For the outer muon station, the DT  
 424 chamber contains only 8 layers of DT cells, providing a muon position in the  $r\phi$  plane. There are

425 four CSC stations in each end cap, providing muon measurements for  $0.9 < |\eta| < 2.4$  (Run I  
 426 configuration). These CSC are multi-wired proportional chambers that consist of 6 anode wire  
 427 planes crossed by 7 copper strips cathode panels in a gas volume. The  $r$  coordinate is provided  
 428 by the copper strips, while  $\phi$  coordinate comes from the anode wires, giving a two dimensional  
 429 position measurement. There are six layers of RPC in the barrel muon system and one layer into  
 430 each of the first three stations of the end cap. They are made from two high resistive plastic  
 431 plates with an applied voltage and separated by a gas volume. Read out strips mounted on top  
 432 of the plastic plates detect the signal generated by a muon passing through the gas volume. The  
 433 RPC provides a fast response with a time resolution of 1 ns and covers a range of  $|\eta| < 1.8$   
 434 (Run I configuration).

435 During the LS1, the muon system underwent major upgrades [63, 64]. In the fourth station  
 436 of each end cap, the outermost rings of CSC and RPC chambers were completed, providing an  
 437 angular region of  $1.2 < |\eta| < 1.8$  for Run II, increasing the system redundancy, and allowing  
 438 tighter cuts on the trigger quality. In order to reduce the environmental noise, outer yoke discs  
 439 have been placed on both sides for the end caps. At the innermost rings of the first station, the  
 440 CSC has been upgraded by refurbishing the readout electronics to make use of the full detector  
 441 granularity instead of groups of three (Run I).

442 The muon system provides triggering on muons, identifying muons and improves the momen-  
 443 tum measurement and charge determination of high  $p_T$  muons. On top of the muon system,  
 444 the muon energy is deposited in the electromagnetic calorimeter, the hadronic calorimeter, and  
 445 outer calorimeter. The high magnetic field enables an efficient first level trigger and allows a  
 446 good momentum resolution of  $\Delta p/p \approx 1\%$  for a  $p_T$  of 100 GeV and  $\approx 10\%$  for a  $p_T$  of 1 TeV  
 447 (FIXME). There is an efficient muon measurement up to  $|\eta| < 2.4$ .

#### 448 Muon reconstruction

449 The muon reconstruction[65] has three subdivision: local reconstruction, regional reconstruction  
 450 and global reconstruction. The local reconstruction is performed on individual detector elements  
 451 such as strip and pixel hits in the inner tracking system, and muon hits and/or segments  
 452 on the muon chambers. Independent tracks are reconstructed in the inner tracker - called  
 453 tracker track - and in the muon system, called standalone tracks. Based on these tracks,  
 454 two reconstructions are considered. The outside-in approach is referred to as Global Muon  
 455 reconstruction. For each standalone track, a tracker track is found by comparing the parameters  
 456 of the two tracks propagated onto a common surface. Combining the hits from the tracker  
 457 track and the standalone track, gives a fit via the Kalman filter technique [66, 67] for a global  
 458 muon track. The second approach is an inside-out reconstruction, creating tracker muons. All  
 459 candidate tracker tracks are extrapolated to the muon system taking into account the magnetic  
 460 field, the average expected energy losses, and multiple Coulomb scattering in the detector  
 461 material. When at least one muon segment - DT or CSC hits - matches the extrapolated track,  
 462 the corresponding tracker track is indicated as a tracker muon.

463 For low transverse momenta ( $p_T \lesssim 5$  GeV), the tracker muon reconstruction is more efficient  
 464 than the global muon approach. This is due to the fact that tracker muons only require a  
 465 single muon segment in muon system, while the global muon approach requires typically

466 segments in at least two muon stations. The global muon approach typically improves the  
 467 tracker reconstruction for  $p_T \gtrsim 200$  GeV.

468 **2.2.2.2 Solenoid**

469 Making use of the knowledge of previous experiments of ALEPH and DELPHI at LEP and H1  
 470 at HERA, CMS choose for a large super conducting solenoid with a length of 12.9 m and  
 471 a inner bore of 5.9 m[58]. With 2 168 turns, a current of 19.5 kA and a total energy of 2.7  
 472 GJ, a large bending power can be obtained for a modestly-sized solenoid. In order to ensure a  
 473 good momentum resolution in the forward regions, a favourable length/radius was necessary.  
 474 In [Figure 2.7](#), a photo of the CMS solenoid is given.

475 The solenoid uses a high-purity aluminium stabilised conductor with indirect cooling from  
 476 liquid helium, together with fully epoxy impregnation. A four-layer winding is implemented that  
 477 can withstand an outward pressure of 64 atm. The NbTi cable is co-extruded by pure aluminium  
 478 that acts as a thermal stabilizer and has an aluminium alloy for mechanical reinforcement. The  
 479 return of the magnetic field is done by fives wheels, noted by YB in [Figure 2.5](#).

480 **2.2.2.3 Hadronic calorimeter**

481 The hadronic calorimeter (HCAL) is dedicated to precisely measure the energy of charged and  
 482 neutral hadrons via a succession of absorbers and scintillators. This makes it crucial for physics  
 483 analyses with hadronic jets or missing transverse energy. The HCAL extends between 1.77  
 484  $< r < 2.95$  m where  $r$  is the radius in the transverse plane with respect to the beam. Due  
 485 to space limitations, the HCAL needs to be as small as possible and is made from materials  
 486 with short interaction lengths - the length needed for absorbing 36.7% of the hadrons. The  
 487 quality of the energy measurements is dependant on the fraction of the hadronic shower that  
 488 can be detected. Therefore, the HCAL barrel (HB) inside the solenoid is reinforced by an outer  
 489 hadronic calorimeter between the solenoid and muon detectors (HO, see [Figure 2.8](#)), using the  
 490 solenoid as extra absorber. This increases the thickness to 12 interaction lengths. Furthermore,  
 491 it should be as hermetic as possible and extend to large pseudo rapidity values. The HB and HO  
 492 provide measurements for  $|\eta| < 1.3$ , while an end cap on each side (HE,  $1.3 < |\eta| < 3$ ) and a  
 493 forward calorimeter (HF,  $|\eta| < 5.2$ ) extend the pseudo rapidity range.

494 The HB is made of 16 absorber plates where most of them are built from brass and others  
 495 are made from stainless steal and is about five to ten intercation lengths thick. The HE is also  
 496 composed of brass absorber plates and has a thickness corresponding to approximately ten  
 497 interaction lengths. The HF experiences intense particle fluxes with an energy of 760 GeV  
 498 deposited on average in a proton interaction at a center of mass of 14 TeV, compared to 100  
 499 GeV in the rest of the detector. Therefore, these are Cherenkov light detectors made of radiation  
 500 hard quartz fibers. The main causes of such large energy events are high energy muons, cosmic  
 501 particles and charged particles from late showering hadrons. During Run I, it became clear that  
 502 the glass windows of the PMTs had to be replaced which was done during LS1 [68]

503 **2.2.2.4 Electromagnetic calorimeter**

504 The electromagnetic calorimeter (ECAL) is designed to measure the energy of photons and  
 505 electrons and covers  $|\eta| < 3$ . It is an hermetic, homogeneous detector and consists of 75 848

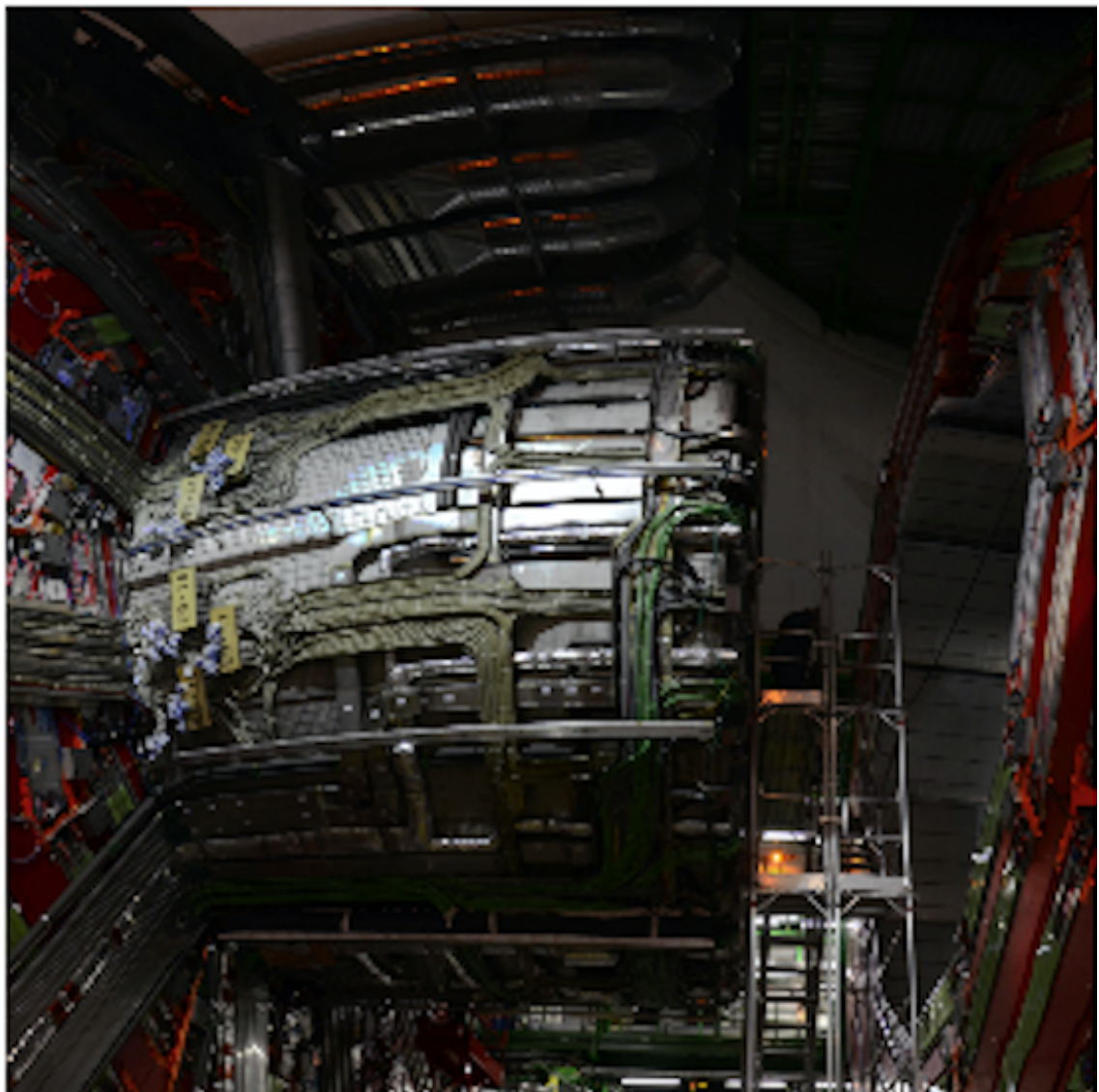


Figure 2.7: CMS solenoid during the long shutdown in 2013.

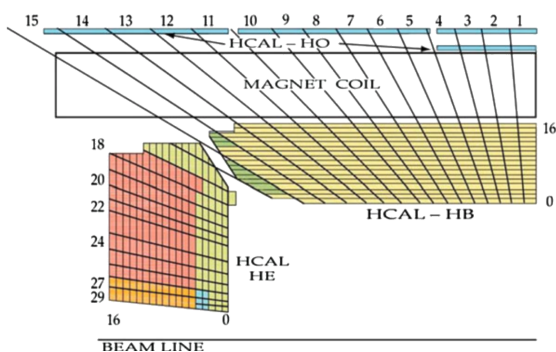
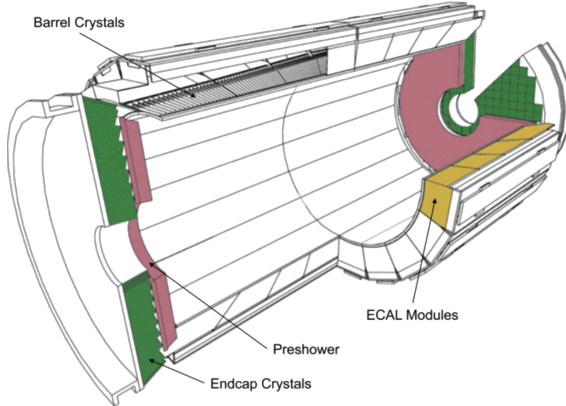


Figure 2.8: Tower segmentation for one quarter of the HCAL displayed in the  $rz$  plane[48].

506 lead tungstate ( $\text{PbWO}_4$ ) crystals. These crystals have a fast response time - 80% of the light  
 507 is emitted within 25 ns - and are radiation hard. The electromagnetic showers produced by  
 508 passing electrons or photons ionize the crystal atoms which emit a blue-green scintillation light,  
 509 that is collected by silicon avalanche photodiodes (APDs) in the barrel and vacuum phototriodes  
 510 (VPTs) in the end caps. The crystals and the APD response is sensitive to temperature changes  
 511 and require a stable temperature.



**Figure 2.9:** Schematic cross section of the electromagnetic calorimeter[48].

512 There are three regions: a central barrel (EB), a endcap region (EE) and a preshower (ES)  
 513 (Figure 2.9). The EB has an inner radius of 129 cm and corresponds to a pseudo rapidity of  
 514  $0 < |\eta| < 1.479$ . At a distance of 314 cm from the vertex and covering a pseudo rapidity  
 515 of  $1.479 < |\eta| < 3.0$ , are the EE. They consist of semi-circular aluminium plates from which  
 516 structural units of  $5 \times 5$  crystals (super crystals) are supported. The ES is placed in front of  
 517 the crystal calorimeter over the end cap pseudo rapidity range with two planes of silicon strip  
 518 detectors as active elements.

The electromagnetic shower will typically involve more than one channel. More than 90% of the energy of a 35 GeV electron or photon is contained in a  $5 \times 5$  matrix of crystals. Therefore, a clustering algorithm is performed in order to associate the energy deposits to the particles impinging the calorimeter. The achieved precision[69] for the barrel is  $2.10^{-3}$  rad in  $\phi$  and  $10^{-3}$  in  $\eta$ . For the end caps this is  $5.10^{-3}$  rad in  $\phi$  and  $2.10^{-3}$  in  $\eta$ . The energy is reconstructed by a super cluster algorithm, taking into account energy radiated via bremsstrahlung or conversion:

$$E_{e/\gamma} = GF_{e/\gamma} \sum_{i \in \text{cluster}} S_i(t)VC_iA_i, \quad (2.5)$$

where  $G$  is the absolute energy scale in GeV/ADC,  $F$  the energy containment corrections (depends on type of particle, its energy and pseudo rapidity, eg shower leakage and bremsstrahlung losses for electrons),  $S(t)$  the relative channel variation with time,  $C$  the relative channel response and  $A$  the amplitude in ADC counts. The energy resolution is given by

$$\frac{\sigma(E)}{E} = \frac{2.8\%}{\sqrt{E}} \oplus \frac{0.128}{E(\text{GeV})} \oplus 0.3\%, \quad (2.6)$$

519 in the absence of a magnetic field, where the contributions come from the stochastic, noise and  
 520 constant terms respectively. The dominating term is the constant term ( $E_{shower} \approx 100\text{GeV}$ ) and  
 521 thus the performance is highly dependent on the quality of calibration and monitoring .

522 In Run I, the energy reconstruction happened via a weighted sum of the digitized samples[70].  
 523 For Run II however, the reconstruction had to be made more resistant for out of time pile up  
 524 and a multi-fit approach has been set in to place. In this approach, the pulse shape is modelled  
 525 as a sum of one in-time pulse plus the out of time pulses [69]. The energy resolution is less  
 526 than 2% in the central barrel region and 2-5 % elsewhere.

### 527 2.2.2.5 Inner tracking system and operations

528 The tracking system (tracker) [71] is the detecting unit closest to the point of interaction.  
 529 Responsible for the reconstruction of trajectories from charged particles with  $|\eta| < 2.5$  that are  
 530 bent by the magnetic field, it provides a measurement of the momentum. The tracker is also  
 531 responsible for the determination of the interaction point or vertex. It should be able to provide  
 532 high granularity as well as speed, and be able to endure high radiation. For this reason, the  
 533 CMS collaboration choose silicon detector technology.

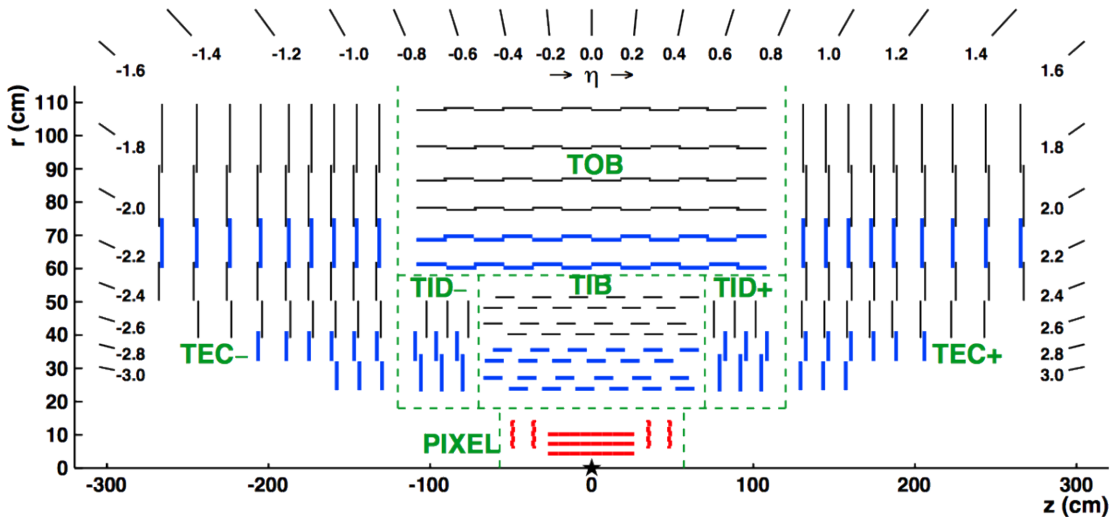


**Figure 2.10:** Schematic cross section of the top half of the CMS tracking system in the  $r$ - $z$  plane. The centre of tracker is shown with a star and corresponds to the approximate position of the proton collision point. The green dashed lines are an indication for each named tracker subsystem. The strip tracker modules that provide two-dimensional hits are shown by thin, black lines, while those able to reconstruct three-dimensional hit positions are shown by thick, blue lines. The pixel modules, shown in red, also provide three-dimensional hits. [57]

534 The tracking system consists of a cylinder of 5.8 m long and 2.5 m in diameter. It is immersed  
 535 in a co-axial magnetic field of 3.8 T due to the solenoid. As shown Figure 2.10, the tracker  
 536 is built up from a large silicon strip tracker with a small silicon pixel inside. The inner region,  
 537 pixel ( $4.4 < r < 10.2$  cm), gets the highest flux of particles. Therefore, pixel silicon sensors  
 538 of  $100 \times 150$   $\mu\text{m}$  area used. It consists of three cylindrical barrels that are complemented by

539 two discs of pixel modules at each side. The silicon strip tracker ( $20 < r < 116$  cm) has three  
 540 subdivisions. The Tracker Inner Barrel and Discs (TIB, TID, see [Figure 2.12](#)) are composed  
 541 of four barrel layers accompanied by three discs at each end. The outer part of the tracker -  
 542 Tracker Outer Barrel (TOB) - consists of 6 barrel layers. In the outer discs, there are nine discs  
 543 of silicon sensors, referred to as Tracker End Caps (TEC).

544 The pixel, shown in [Figure 2.11](#) has 1440 modules that cover an area of about  $1\text{ m}^2$  and have  
 545 66 million pixels. It provides a three-dimensional position measurement of the hits arising from  
 546 the interaction from charged particles with the sensors. In transverse coordinate ( $r\phi$ ), the hit  
 547 position resolution is about  $10\text{ }\mu\text{m}$ , while  $20\text{-}40\text{ }\mu\text{m}$  is obtained in the longitudinal coordinate  
 548 ( $z$ ). The sensor plane position provides the third coordinate. The silicon strip trackers consists  
 549 of 15 148 single sided modules placed in the TIB, TID and the first four rings of the TEC.  
 550 They provide 9.3 million readout channels. In the TOB and the outer three rings of the TEC,  
 551 double sided modules are used. These modules are constructed from two back-to-back single  
 552 sided modules, where one module is rotated through a stereo angle. This covers an active area  
 553 of about  $198\text{ m}^2$ . The TIB and TID provide position measurements in  $r\phi$  with a resolution of approximately  
 554  $13\text{-}38\text{ }\mu\text{m}$ , while the TOB provides a resolution of about  $18\text{-}47\text{ }\mu\text{m}$ . The  
 555 resolution in the  $z$  direction is approximately  $230\text{ }\mu\text{m}$  in the TIB/TID and  $530\text{ }\mu\text{m}$  in the TOB.  
 556 To allow overlay and avoid gaps in acceptance, each module is shifted slightly in  $r$  or  $z$  with  
 557 respect to its neighbouring modules within a layer. With this detector lay out, at least nine  
 558 points per charged particle trajectory can be measured in an  $|\eta|$  range up to 2.4.

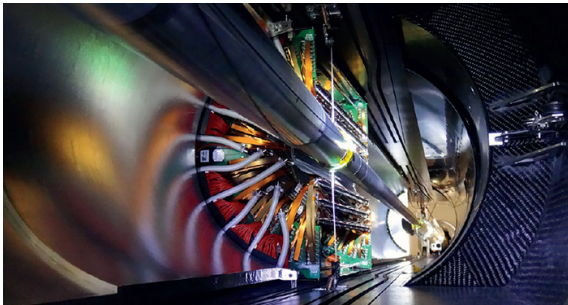


**Figure 2.11:** The pixel barrel being re-installed after the Long Shutdown in 2015, around the beam pipe at CMS [72]

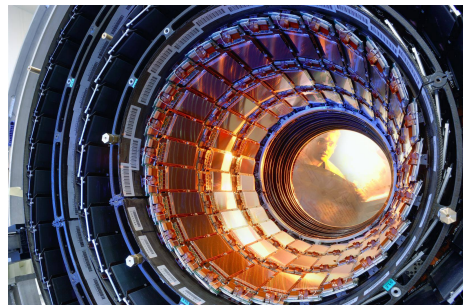


**Figure 2.12:** First half of the inner tracker barrel, consisting of three layers of silicon modules [73].

During the first data taking period of the LHC (2010 to 2013), the tracker operated at  $+4^\circ\text{C}$ . With the higher LHC beam intensities from 2015 onwards, the tracker needs to be operated at much lower temperatures. This is due to the fact with intense irradiation, the doping concentration changes, the leakage current increases proportional to the fluence and the charge collection efficiency decreases due to charge trapping. Mostly the leakage current ( $I$ ) is affected by the temperature change:

$$I \propto T^2 e^{-\frac{E_g}{2kT}}, \quad (2.7)$$

559 where  $T$  is the operating temperature,  $E_g$  the band gap and  $k$  the Boltzmann constant. There is  
 560 approximately a factor 15 between the leakage currents at room temperatures and at  $-10^\circ\text{C}$ .

561 During the LS1, the CMS cooling plant was refurbished[74](Figure 2.14) and the fluorocarbon  
 562 cooling system overhauled. To help to suppress the humidity inside the tracker, new methods  
 563 for vapour sealing and insulation were applied (Figure 2.13). Furthermore, several hundred  
 564 high-precision sensors are used to monitor the humidity and temperature. In order to get as  
 565 dry air as possible, a new dry-gas plant provides eight times more dry gas (air or nitrogen)  
 566 than during the first run, and allows regulation if the flow. As final addition, the cooling  
 567 bundles outside the tracker are equipped with heater wires and temperature sensors in order to  
 568 maintain safe operations above the cavern dew point For the data taking in 2015-2016, the  
 569 tracker operated at  $-15^{\circ}\text{C}$ .

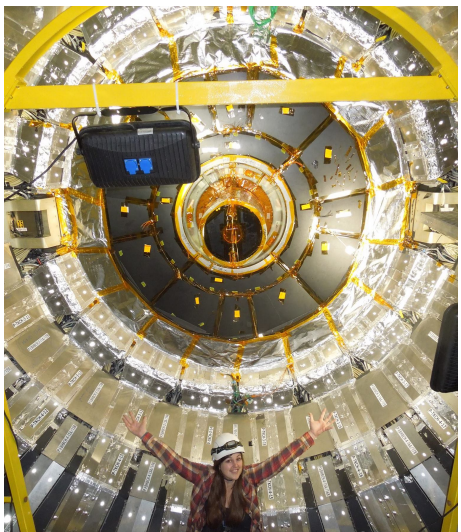


**Figure 2.13:** Tracker bulkhead being put into closed state with insulation pieces installed during an early trial in fall 2013



**Figure 2.14:** New Tracker high-capacity dry-gas plant with membrane separation system [61].

## 570 Track reconstruction

571 An iterative tracking algorithm is responsible for the reconstruction of the tracks made by  
 572 charged particles in the inner tracking system. Each iteration consists of four steps[58]: the  
 573 track-seed generation, the pattern recognition algorithm, removal of track-hit ambiguities and  
 574 a final track fit.

575 The seed generation is the first step. It consists of finding reconstructed hits that are usable  
 576 for seeding the subsequent track-finding algorithm. They are identified from a group of at  
 577 least three reconstructed hits in the tracker, or from a pair of hits while requiring the origin  
 578 of the track segment to be compatible with the nominal beam-collision point. Since the pixel  
 579 has a higher granularity compared to the strip tracker, its seed generation efficiency is higher.  
 580 The overall efficiency exceeds 99%. The second step of each iteration, the pattern recognition  
 581 algorithm, uses the seeds as a starting point for a Kalman filter method [66, 67]. This algorithm  
 582 extrapolates the seed trajectory towards the next tracker layer taking into account the magnetic  
 583 field and multiple scattering effects. The track parameters are updated when a compatible hit

584 in the next layer is found. This procedure continues until the outermost layer is reached. Since  
 585 the Kalman filter method can result in multiple tracks associated to the same seed, or different  
 586 tracks sharing the same hits, a removal of ambiguities is necessary. This ambiguity resolving is  
 587 done by removing tracks that are sharing too many hits from the list of track candidates. The  
 588 tracks with highest number of hits or with the lowest  $\chi^2$  if the track fit is kept. The updated  
 589 track parameters are then refitted using the Kalman filter method, where all hits found in the  
 590 pattern recognition step are taken into account. The fit is done twice - once outwards from the  
 591 beam line towards the calorimeters, and inwards from the outermost track hit to the beam line  
 592 -, improving the estimation of the track parameters.

593 All hits that are unambiguously associated to the final track are removed from the list of  
 594 available hits. In order to associate the remaining hits, the procedure is repeated with looser  
 595 track reconstruction criteria. The use of the iterative track reconstruction procedure has a  
 596 high track finding efficiency, where the fake track reconstruction rate is negligible. For muons,  
 597 this results in a global track reconstruction efficiency exceeding 98%, and 75-98% for charged  
 598 hadrons.

### 599 Primary vertex reconstruction

600 The primary vertex reconstruction should be able to measure the location of all proton interaction  
 601 vertices in each event: the signal vertex and all vertices from pile up events. It consists of a vertex  
 602 finding and a vertex fitting algorithm and happens in three steps. Tracks are selected to be  
 603 consistent with being produced promptly in the primary interaction by imposing requirements  
 604 on the track parameters[71] By grouping reconstructed tracks according to the z coordinate of  
 605 their closest approach to the beam line, vertices for all interaction in the same beam crossing  
 606 are found, at CMS this is done by a deterministic annealing algorithm [75] . On top of this,  
 607 a vertex fitting algorithm like the Adaptive Vertex fitter [76], is performed. This creates the  
 608 three-dimensional primary-vertex position. With this fit, the contribution from long-lived hadron  
 609 decays is reduced by down weighting the tracks with a larger distance to the vertex. The primary  
 610 vertex corresponding to the highest sum of squared track transverse momenta is noted as the  
 611 point of the main interaction. The resolution on the primary vertex is about 14  $\mu\text{m}$  in  $r\phi$  and  
 612 about 19  $\mu\text{m}$  in the z direction for primary vertices with the sum of the track  $p_T > 100$  GeV  
 613 for 2016 data taking.

### 614 2.2.3 Data acquisition

615 At a design luminosity of  $10^{34} \text{ 1}/(\text{m}^2 \text{ s})$ , the proton interaction rate exceeds 1 GHz. This makes  
 616 it impossible for the CMS experiment to store all the data generated. For this, a two level trigger  
 617 system has been put in place. The first level (Level-1) is a custom hardware system, while a  
 618 second level (HLT) is software based running on a large farm of computers. In run II, with the  
 619 increase in centre of mass energy and a higher luminosity, a larger number of simultaneous  
 620 inelastic collisions per crossing is expected with respect to run I. For this, the CMS Level-1 has  
 621 been upgraded [77].

622 **CMS Level-1 trigger**

623 The Level-1 trigger has to be a flexible, maintainable system, capable of adapting to the evolving  
 624 physics programme of CMS [78]. Its output rate is restricted to 100 kHz imposed by the CMS  
 625 readout electronics. It is implemented by custom hardware and selects events containing candi-  
 626 date objects - eg ionization deposits consistent with a muon, or energy clusters corresponding  
 627 to an electron / photon / tau lepton / missing transverse energy / jet. Collisions with large  
 628 momenta can be selected by using scalar sum of the transverse momenta of the jets.

629 By buffering the raw data from the CMS subdetectors in front-end drivers, the level-1 trigger  
 630 has a pipeline memory of 3.2  $\mu$ s to decide whether to keep an event or reject it. The trigger  
 631 primitives (TP) from the calorimeters and muon detectors are processed in several steps and  
 632 combined into a global trigger. This information is then combined with the input from the other  
 633 subsystems for the HLT. The separate inputs are synchronized to each other and the LHC orbit  
 634 clock and sent to the global trigger module. Here, level-1 trigger algorithms are performed  
 635 within 1  $\mu$ s to decide whether to keep the event.

636 For run II, all hardware, software, databases and the timing control system have been replaced.  
 637 The main changes are that the muon system now uses the redundancy of three muon detector  
 638 system earlier to make a high resolution muon trigger. Other upgrades are that the calorimeter  
 639 system isn't bound any more for streaming data the data and the global trigger has more level-1  
 640 trigger algorithms.

641 **CMS HLT trigger**

642 The HLT is an array of commercially available computers with programmable menu that has  
 643 output rate of on average 400 Hz for off-line event storage. The data processing is based on a  
 644 HLT path. This is a set of algorithmic steps to reconstruct objects and make selections on them.  
 645 Here, the information of all sub detectors can be used to perform algorithms on higher level  
 646 reconstructed objects.

647 **2.2.4 CMS computing model**

648 The selected data is stored, processed and dispersed via the Worldwide Large Hadron Collider  
 649 GRID (WLCG)[79, 80]. This has a tiered structure that function as a single, coherent system:

650 At CERN, a single Tier-0 is located. The raw data collected by CMS is archived here, and  
 651 a first reconstruction of the data is done. This data is then already in a file format usable for  
 652 physics analysis. Furthermore, it is able to reprocess data when new calibrations are made  
 653 available. The Tier-0 site distributes this data to a total of seven Tier-1 centres. They carry out  
 654 data reprocessing and store real data as well as simulated data. The Tier-1 further distribute  
 655 the data to over 50 Tier-2 centres. These make the data accessible for physics analysis and are  
 656 also being used for the production of simulated data. The data is made accessible for physicists  
 657 around the world.

658

# Analysis techniques

# 3

659

**NOTE:**  
Write introduction to  
this chapter

660

## 3.1 Hadron collisions at high energies

In hadron collisions at sufficiently high momentum transfer, all partons can be approximated as free making it possible to treat hadron-hadron scattering as a single parton-parton interaction. The momentum of the parton can then be expressed as a fraction of the hadron momentum

$$\vec{p}_{\text{parton}} = x \vec{p}_{\text{hadron}}, \quad (3.1)$$

where  $x$  is referred to as the Björken scaling variable. The interaction  $p_A p_B \rightarrow X$  can then be factorised in terms of partonic cross sections  $\hat{\sigma}_{ij \rightarrow X}$  [81]

$$\sigma_{p_A p_B \rightarrow X} = \sum_{ij} \iint dx_1 dx_2 f_i^A(x_1, Q^2) f_j^B(x_2, Q^2) d\hat{\sigma}_{ij \rightarrow X}, \quad (3.2)$$

661 where  $i$  and  $j$  are the partons resolved from protons A and B,  $f_i(x_i, Q^2)$  the parton density  
 662 functions (PDF), and  $Q^2$  the factorisation scale more commonly denoted as  $\mu_F$ . The factorisation  
 663 scale is the scale at which the hadronic interaction can be expressed as a product of the partonic  
 664 cross section and the process independent PDF. In Figure 3.1, the kinematic regions in  $x$  and  
 665  $\mu_F$  are shown for fixed target and collider experiments.

666 The parton density functions (PDF) [82–84] give the momentum distribution of the proton  
 667 amongst its partons at an energy scale  $\mu_F$ . These functions can not be determined from first  
 668 principles and have to be obtained from global fits to data. The PDFs are obtained from measure-  
 669 ments on deep inelastic scattering using lepton-proton collision by the HERA collider [85],  
 670 supplemented with proton-antiproton collisions from Tevatron at Fermilab [86], and proton  
 671 collision data from the ATLAS, CMS and LHCb collaborations at the LHC (Run 1) [87]. These  
 672 measurements are included in global PDF sets known as the PDF4LHC recommendation [84].  
 673 From their measurement at scale  $\mu_F$  these PDFs can be extrapolated using the DGLAP equations  
 674 . The PDFs are used to calculate the cross section of a certain process and are therefore used  
 675 as input for the Monte Carlo generators used to make the simulated data samples at the LHC.  
 676 In the framework of this thesis, the NLO PDF4LHC15\_100 set is used. This set is an envelope

**NOTE:** Add source

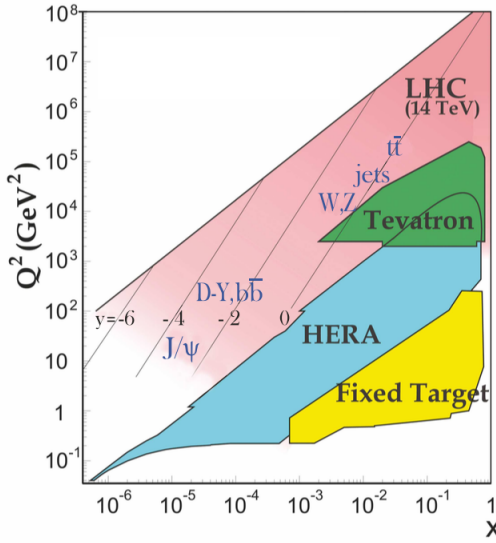


**Figure 3.1:** Kinematic regions in momentum fraction  $x$  and factorisation scale  $Q^2$  probed by fixed-target and collider experiments. Some of the final states accessible at the LHC are indicated in the appropriate regions, where  $y$  is the rapidity. In this figure, the incoming partons have  $x_{1,2} = (M/14\text{TeV})e^{\pm y}$  with  $Q = M$  where  $M$  is the mass of the state shown in blue in the figure. For example, exclusive  $J/\psi$  and  $\Upsilon$  production at high  $|y|$  at the LHC may probe the gluon PDF down to  $x \sim 10^{-5}$ . Figure taken from [4].

of three sets, CT14, MMHT2014 and NNPDF3.0 [84]. In Figure 3.2 the dependency of the PDFs on the momentum fraction  $x$  is shown for the NNPDF3.0 set on hadronic scale ( $\mu_F^2 = (10\text{GeV})^2$ ) and LHC scale ( $\mu_F^2 = (10^4\text{GeV})^2$ ). For most values of the momentum fraction, the gluon density dominates, meaning that it is easier to probe muons than the quarks. For  $x$  close to one, the parton densities of the up and down quarks (the valence quarks of the proton) dominate over the gluon density. The charm, anti-up, and anti-down quarks have lower densities in general since those are sea quarks which originate in the proton only through gluon splitting. The resolution scale  $Q^2$  is typically taken to be the energy scale of the collision. For the top quark pair production a scale of  $Q^2 = (350\text{GeV})^2$  is chosen, meaning that the centre-of-mass energy of the hard interaction is about twice the top quark mass. The uncertainty on the parton distributions is evaluated using the Hessian technique [88], where a matrix with a dimension identical to the number of free parameters needs to be diagonalised. In the case of PDF4LHC15\_100 set, this translates into 100 orthonormal eigenvectors and 200 variations of the PDF parameters in the plus and minus direction.

At high energies divergences can appear from quantum fluctuations. For the theory still to be able to describe the experimental regime, a renormalization scale  $\mu_R$  is used to redefine physical quantities. A consequence of this method is that the coupling constants will run as function of  $\mu_R$ . Beyond this scale, the high energy effects such as the loop corrections to propagators (self energy) are absorbed in the physical quantities through a renormalization of the fields. In

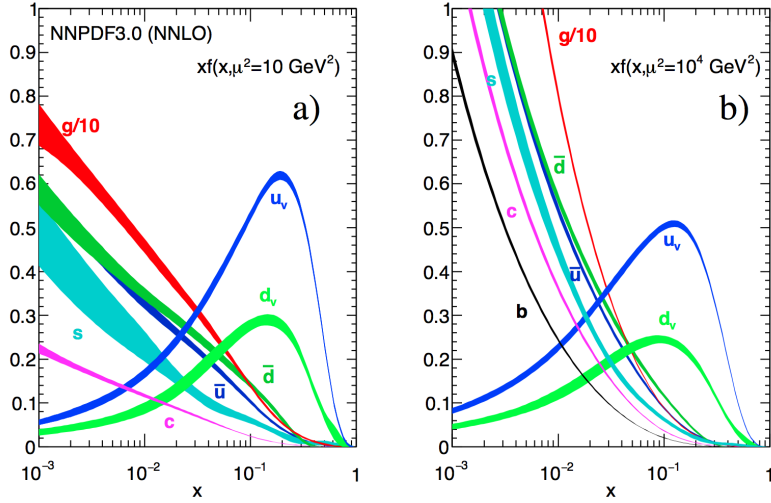


**Figure 3.2:** The momentum fraction  $x$  times the parton distribution functions  $f(x)$ , where  $f = u_v, d_v, \bar{u}, \bar{d}, s, c$ , or  $g$  as function of the momentum fraction obtained in the NNLO NNPDF3.0 global analysis at factorisation scales  $\mu^2 = 10 \text{ GeV}^2$  (left) and  $\mu^2 = 10^4 \text{ GeV}^2$  (right), with  $\alpha_s(M_Z^2) = 0.118$ . The gluon PDF has been scaled down by a factor of 0.1. Figure taken from [4].

particular the running behaviour of the strong coupling constant<sup>1</sup>  $\alpha_s$  is found to be

$$\alpha_s = \frac{\alpha_s(\mu_0^2)}{1 + \alpha_s(\mu_0^2) \frac{33-2n_f}{12\pi} \ln\left(\frac{|\mu_R^2|}{\mu_0^2}\right)}, \quad (3.3)$$

with  $n_f$  the number of quarks and  $\mu_0$  the reference scale on which the coupling is known. The current world average of the strong coupling constant at the Z boson mass is  $\alpha_s(\mu_F = m_Z) = 0.1181 \pm 0.0011$  [4]. From Equation 3.3 one can see easily that the coupling strength decreases with increasing renormalization scale, this known as asymptotic freedom. Additionally, following the behaviour of  $\alpha_s(\mu_R^2)$ , a limit  $\Lambda_{\text{QCD}} \approx 200 \text{ MeV}$  is found for which  $\alpha_s$  becomes larger than one. Under this limit, the perturbative calculations of observables can no longer be done.

Cross sections be written in terms of interacting vertices contributing to the matrix element (ME) originating from elements of a perturbative series [89], allowing them to be expanded as a power series of the coupling constant  $\alpha$

$$\sigma = \sigma_{\text{LO}} \left( 1 + \left( \frac{\alpha}{2\pi} \right) \sigma_1 + \left( \frac{\alpha}{2\pi} \right)^2 \sigma_2 + \dots \right). \quad (3.4)$$

Leading order (LO) accuracy contains the minimal amount of vertices in the process, then depending on where the series is cut off one speaks of next-to-leading order (NLO), or next-to-next-to-leading order (NNLO) accuracy in  $\alpha$ . Predictions including higher order correction tend to be less affected by theoretical uncertainties originating from a variation of the chosen renormalization and factorisation scales.

<sup>1</sup>The strong coupling constant is defined as  $\alpha_s = \frac{g_s^2}{4\pi}$ .

## 702 3.2 Event generation

703 In order to compare reconstructed data with theoretical predictions, collision events are gen-  
 704 erated and passed through a simulation of the CMS detector and an emulation of its readout.  
 705 For the detector simulation, a so-called Full Simulation package [90, 91] based on the Geant4  
 706 toolkit [92] is employed. It allows a detailed simulation of the interactions of the particles with  
 707 the detector material.

### 708 3.2.1 Fundamentals of simulating a proton collision

709 The procedure of to generate  $pp \rightarrow X$  events can be subdivided into sequential steps [93–95],  
 as shown in Figure 3.3.

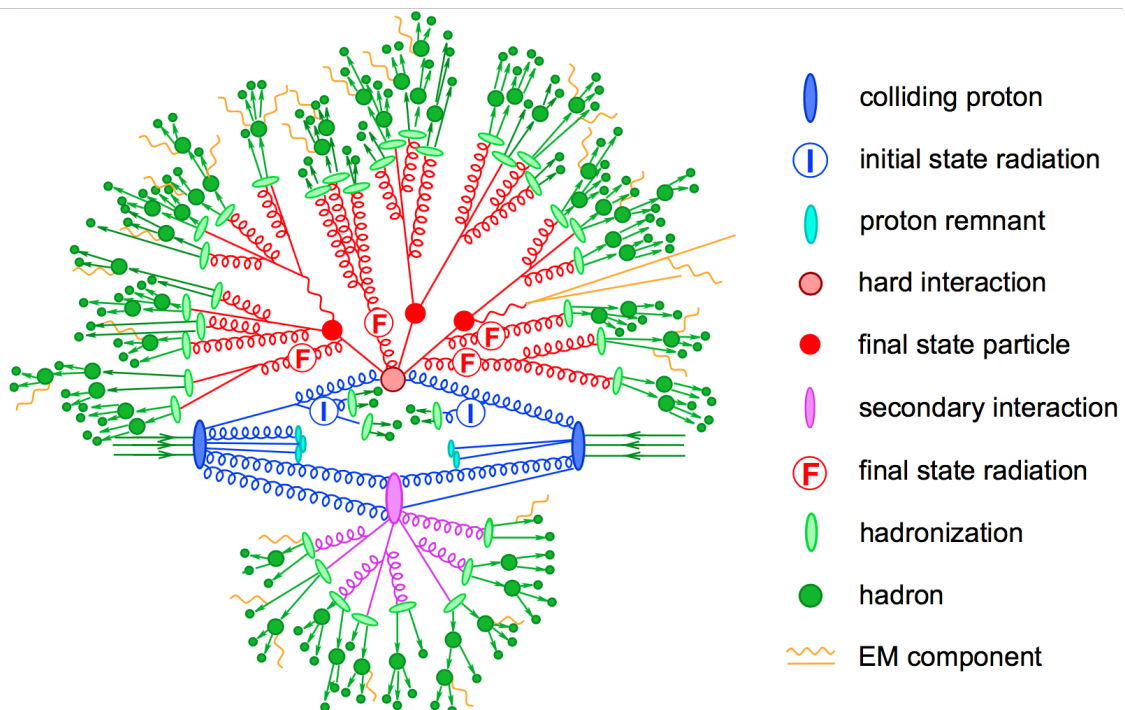


**Figure 3.3:** Sketch of a hadron collision as simulated by a Monte-Carlo event generator. The red blob in the centre represents the hard collision, surrounded by a tree-like structure representing Bremsstrahlung as simulated by parton showers. The purple blob indicates a secondary hard scattering event. Parton-to-hadron transitions are represented by light green blobs, dark green blobs indicate hadron decays, while yellow lines signal soft photon radiation. Figure taken from [95].

710

711 The interaction of two incoming protons is often soft and elastic leading to events that are not  
 712 interesting in the framework of this thesis. More intriguing are the hard interaction between two  
 713 partons from the incoming protons. The matrix elements of a hard scattering process of interest  
 714 is the starting point of the generation of events. Monte Carlo techniques are used to sample the  
 715 corresponding cross section integral and the resulting sample of events reflect the probability  
 716 distribution of a process over its final state phase space. After obtaining the sample of events of  
 717 the hard interaction, a parton shower (PS) program is used to simulate the hadronisation of

718 final state partons into hadrons which then decay further. Additionally, radiation of soft gluons  
 719 or quarks from initial or final state partons is simulated. These are respectively referred to as  
 720 initial state radiation (ISR) or final state radiation (FSR). Contributions from soft secondary  
 721 interactions, the so-called underlying event (UE), and colour reconnection effects are also taken  
 722 into account. A brief overview of the employed programs used for the event generation of the  
 723 signal and main background processes used in the search presented in the thesis are given in  
 724 [Section 3.2.2](#).

**NOTE:**  
Should I  
add more  
details?

### 725 3.2.2 Programs for event generation

726 The FEYNRULES package [96] allows the calculation of the Feynman rules in momentum space  
 727 for any quantum field theory model. By use of a Lagrangian, the set of Feynman rules associated  
 728 with this Lagrangian are calculated. Via the Universal FeynRules Output (UFO) [97] the  
 729 results are then passed to matrix element generators.

730 The MadGraph program [98] is used to interpret the physics model and calculate the cor-  
 731 responding Feynman diagrams and matrix elements. After this, MadEvent [99] is used to  
 732 calculate the corresponding partons. These generated parton configurations are then merged  
 733 with Pythia [100–102] parton showers using the MLM merging scheme [103].

734 The MadGraph5\_aMC@NLO program [104] combines the LO MadGraph [98] and the aMC@NLO  
 735 program into a common framework. This combination supports the generation of samples at  
 736 LO or next to NLO together with a dedicated matching to parton showers using the MLM [103]  
 737 or FXFX [105] schemes respectively. The FXFX scheme produces a certain fraction of events  
 738 with negative weights originating from the subtraction of amplitudes that contain additional  
 739 emissions from the NLO matrix element to prevent double-counting.

740 The POWHEG box (versions 1,2) [106–111] contains predefined implementations of various  
 741 processes at NLO. It applies the POWHEG method for ME- to PS- matching, where the hardest  
 742 radiation generated from the ME has priority over subsequent PS emission to remove the overlap  
 743 with the PS simulation.

744 The JHU generator (version 7.02) [112–115] is used to generate the parton level information  
 745 including full spin and polarization correlations. It is commonly used for studying the spin and  
 746 parity properties of new resonances such as  $ab \rightarrow X \rightarrow VV$ , where  $V = Z, W, \gamma$ .

747 The generation of events from processes involving the production and decay of resonances  
 748 creates a computational heavy load, especially at NLO. The narrow width approximation the  
 749 resonant particle is assumed to be on-shell. This makes the production and decay amplitude  
 750 factorize, allowing to perform the simulation of the production and decay of heavy resonances  
 751 like top quarks or Higgs bosons to be performed in separate steps. The MadSpin program [116]  
 752 extends this approach and accounts for off-shell effects through a partial reweighting of the  
 753 events. Additionally, spin correlation effects between production and decay products are taken  
 754 into account.

755 The Pythia program (versions 6,8) [100–102] generates events of various processes at LO.  
 756 Usually in the analysis, it is however only used for its PS simulation and it is interfaced with

757 other LO and NLO event generators to perform subsequent parton showering, hadronisation,  
 758 and simulation of the underlying event. In this thesis the underlying event tunes [117] are the  
 759 CUETP8M2T4, CUETP8M1 and CUETP8M2.

760 The detector response is simulated via the Geant4 [92] program. This program tracks the  
 761 particles through the detector material via a detailed description of the detector and generates  
 762 several hits throughout several sensitive layers. In addition, the response of the detector  
 763 electronics to these hits are simulated.

### 764 3.2.3 Generating FCNC top-Z interactions

765 The FCNC processes are generated by interfacing the Lagrangian in [Equation 1.25](#) with  
 766 MadGraph5\_aMC@NLO by means of the FeynRules package and its Universal FeynRules  
 767 Output format. The complex chiral parameters are arbitrary chosen to be  $f_{Xq}^L = 0$  and  $f_{Xq}^R = 1$ .  
 768 The signal rates are estimated by use of the MadGraph5\_aMC@NLO program for estimating the  
 769 partial widths. The anomalous couplings are left free to float for this estimation, and only one  
 coupling allowed to be non-vanishing at a time. The results are presented in [Table 3.1](#). The

**Table 3.1:** Leading order partial widths related to the anomalous decay modes of the top quark, where the new physics scale  $\Lambda$  is given in GeV.

Anomalous coupling	vertex	Partial decay width (GeV)
$\kappa_{gqt}/\Lambda$	t g u	$3.665220 \cdot 10^5$ $(\kappa_{tgu}/\Lambda)^2$
	t g c	$3.664620 \cdot 10^5$ $(\kappa_{tgc}/\Lambda)^2$
$\kappa_{t\gamma q}/\Lambda$	t $\gamma$ u	$1.989066 \cdot 10^4$ $(\kappa_{t\gamma u}/\Lambda)^2$
	t $\gamma$ c	$1.988904 \cdot 10^4$ $(\kappa_{t\gamma c}/\Lambda)^2$
$\kappa_{tZq}/\Lambda$	t Z u	$1.637005 \cdot 10^4$ $(\kappa_{tzu}/\Lambda)^2$
	t Z c	$1.636554 \cdot 10^4$ $(\kappa_{tzc}/\Lambda)^2$
$\zeta_{tZq}$	t Z u	$1.685134 \cdot 10^{-1}$ $(\zeta_{tzu})^2$
	t Z c	$1.684904 \cdot 10^{-1}$ $(\zeta_{tzc})^2$
$\eta_{tHq}$	t H u	$1.904399 \cdot 10^{-1}$ $(\eta_{thu})^2$
	t H c	$1.904065 \cdot 10^{-1}$ $(\eta_{thc})^2$

770  
 771 anomalous single top cross sections are calculated by convolution of the hard scattering matrix  
 772 elements with the LO order set of CTEQ6 partons densities [118]. The NLO effects are modelled  
 773 by multiplying each LO cross section by a global  $k$ -factor. The LO single top production cross  
 774 section and the global  $k$ -factors for the top-Z production are shown in [Table 3.2](#). The hard  
 775 scattering events are then matched to parton showers to Pythia to account for the simulation  
 776 of the QCD environment relevant for hadronic collisions.

The top pair cross sections are derived from the SM  $t\bar{t}$  cross section, calculated with MadGraph5\_aMC@NLO at NLO ( $\sigma_{t\bar{t}} = 6.741 \cdot 10^2 \text{ pb}$ ), and considering the decay  $t\bar{t} \rightarrow (bW^\pm)(X_{qt})$ . The branching ratio

**Table 3.2:** Leading order single top production cross section for  $pp \rightarrow tZ$  or  $\bar{t}Z$ , where the new physics scale is given in GeV. The NLO  $k$ -factors [119] are given in the last column.

Anomalous coupling	Cross section (pb)	NLO $k$ -factor
$\kappa_{tg_u}/\Lambda$	$3.272 \cdot 10^7$	$(\kappa_{tg_u}/\Lambda)^2$
$\kappa_{tg_c}/\Lambda$	$3.021 \cdot 10^6$	$(\kappa_{tg_c}/\Lambda)^2$
$\kappa_{t\gamma_u}/\Lambda$	$2.260 \cdot 10^5$	$(\kappa_{t\gamma_u}/\Lambda)^2$
$\kappa_{t\gamma_c}/\Lambda$	$2.654 \cdot 10^4$	$(\kappa_{t\gamma_c}/\Lambda)^2$
$\kappa_{tZ_u}/\Lambda$	$1.728 \cdot 10^6$	$(\kappa_{tZ_u}/\Lambda)^2$
$\kappa_{tZ_c}/\Lambda$	$2.040 \cdot 10^5$	$(\kappa_{tZ_c}/\Lambda)^2$
$\zeta_{tZ_u}$	7.484	$(\zeta_{tZ_u})^2$
$\zeta_{tZ_c}$	1.038	$(\zeta_{tZ_c})^2$

$\mathcal{B}(t \rightarrow bW^\pm)$  is assumed to be equal to one and the FCNC branching ratio is calculated as

$$\mathcal{B}(t \rightarrow qX) = \frac{\Gamma_{t \rightarrow qX}}{\Gamma_t^{\text{SM}} + \Gamma_t^{\text{FCNC}}} \approx \frac{\Gamma_{t \rightarrow qX}}{\Gamma_t^{\text{SM}}}, \quad (3.5)$$

777 where  $\Gamma_{t \rightarrow qX}$  is given in Table 3.1, and the assumption  $\Gamma_t^{\text{FCNC}} \ll \Gamma_t^{\text{SM}}$  is made. In Table 3.3 the resulting NLO cross sections for the top-Z FCNC interactions are given.

**Table 3.3:** Next to leading order top pair cross section for the top-Z FCNC interactions with a full leptonic decay.

Anomalous coupling	Process	Cross section (pb)
$\kappa_{tZ_u}/\Lambda$	$t\bar{t} \rightarrow (b\ell^+\nu)(\bar{u}\ell^+\ell^-)$	$2.727008 \cdot 10^5$
	$t\bar{t} \rightarrow (\bar{b}\ell^-\bar{\nu})(u\ell^+\ell^-)$	$2.727008 \cdot 10^5$
$\kappa_{tZ_c}/\Lambda$	$t\bar{t} \rightarrow (b\ell^+\nu)(\bar{c}\ell^+\ell^-)$	$2.726257 \cdot 10^5$
	$t\bar{t} \rightarrow (\bar{b}\ell^-\bar{\nu})(c\ell^+\ell^-)$	$2.726257 \cdot 10^5$
$\zeta_{tZ_u}$	$t\bar{t} \rightarrow (b\ell^+\nu)(\bar{u}\ell^+\ell^-)$	2.827184
	$t\bar{t} \rightarrow (\bar{b}\ell^-\bar{\nu})(u\ell^+\ell^-)$	2.827184
$\zeta_{tZ_c}$	$t\bar{t} \rightarrow (b\ell^+\nu)(\bar{c}\ell^+\ell^-)$	2.806801
	$t\bar{t} \rightarrow (\bar{b}\ell^-\bar{\nu})(c\ell^+\ell^-)$	2.806801

**NOTE:**  
these partial widths  
are at LO,  
how does  
this relate  
to NLO that  
is used? Or  
is there no  
difference?

778

### 3.2.4 Generating SM background events

780 The SM  $tZ$  events were generated using the MadGraph5\_aMC@NLO generator, interfaced with  
781 Pythia version 8.2 [102] for parton showering and hadronisation. The  $WZ + \text{jets}$ ,  $t\bar{t}Z$ ,  $tZq$ ,

and  $t\bar{t}W$  samples are produced using the MadGraph5\_aMC@NLO(version 5.222) [104], which includes up to one hadronic jet at next to leading order (NLO) QCD accuracy. Other minor background (e.g. WW, ZZ, tWZ and  $t\bar{t}H$ ) are simulated using different generators such as MadGraph [98], MadSpin [116] and JHU [112–115]. All events are interfaced to Pythia for parton shower and hadronisation.

**NOTE:** Add source

The complete list of SM samples is given in Table 3.4, along with their cross sections. The cross sections without a reference are coming from the generator with which the sample has been made, for some of them the uncertainties are provided by the Generator Group. For each MC sample, the integrated luminosity that the sample represents is estimated as the number of simulated events divided by the cross section of the generated process. For processes generated with MadGraph5\_aMC@NLO, the effective number of simulated events is used, taking into account positive and negative event weights. The correction factor for those events is defined as

$$C = \frac{\text{Nb. of pos. weights} + \text{Nb. of neg. weights}}{\text{Nb. of pos. weights} - \text{Nb. of neg. weights}} \times \text{mc baseweight} \quad (3.6)$$

**Table 3.4:** SM MC samples used in this analysis with their corresponding cross section and MadGraph5\_aMC@NLO correction C when applicable. The generators used for each sample are indicated.

Process	Generator	Cross section (pb)	C
$WZ \rightarrow 3\ell\nu$	MadGraph5_aMC@NLO+Pythia	5.26	1.61
$tZq$ with $Z \rightarrow \ell^+\ell^-$	MadGraph5_aMC@NLO+Pythia	0.0758	3.77
$tqH$ with $H \rightarrow ZZ \rightarrow \ell^+\ell^-\ell^+\ell^-$	JHU+Pythia	$8.80 \cdot 10^{-6}$	-
$t\bar{t}W + \text{jets}$ with $W \rightarrow \ell\nu$	MadGraph5_aMC@NLO+MadSpin+Pythia	$0.2043 \pm 0.0020$	1.94
$t\bar{t}Z \rightarrow 2\ell + 2\nu + \text{other}$ , with $m_{\ell\ell} > 10$ GeV	MadGraph5_aMC@NLO+Pythia	$0.2529 \pm 0.0004$	2.15
$t\bar{t}H, \text{no } b\bar{b} \text{ decays}$	POWHEG+Pythia	0.2151	-
$t\bar{t}H, b\bar{b} \text{ decays}$	POWHEG+Pythia	0.2934	-
$WW \rightarrow 2\ell 2\nu$	POWHEG+Pythia	12.178	-
$ZZ \rightarrow 4\ell$	POWHEG+Pythia	0.3366	-
$WZZ$	MadGraph5_aMC@NLO+Pythia	0.05565	1.14
$ZZZ$	MadGraph5_aMC@NLO+Pythia	0.01398	1.17
single top $tWZ$ , with $Z_\mu \rightarrow \ell^+\ell^-$	MadGraph+Pythia	0.001123	-
single top t-channel $\bar{t}$	POWHEG+MadSpin+Pythia	$44.33^{+1.76}_{-1.49}$	-
single top t-channel $t$	POWHEG+MadSpin+Pythia	$26.38^{+1.32}_{-1.18}$	-
single top $\bar{t}W$	POWHEG+Pythia	$35.85 \pm 0.90 \text{ (scale)} \pm 1.70 \text{ (PDF)}$	-
single top $tW$	POWHEG+Pythia	$35.85 \pm 0.90 \text{ (scale)} \pm 1.70 \text{ (PDF)}$	-
$t\bar{t}$	POWHEG+Pythia	$831.76^{+19.77+35.06}_{-29.20-35.06}$	-
$Z/\gamma^* + \text{jets}$ , with $m_{\ell\ell} > 50$ GeV	MadGraph5_aMC@NLO+Pythia	$3 \times (1921.8 \pm 0.6 \pm 33.2)$	1.49
$Z/\gamma^* + \text{jets}$ , with $10 \text{ GeV} < m_{\ell\ell} < 50 \text{ GeV}$	MadGraph+Pythia	18610	-

### 787 3.3 Multivariate analysis techniques: Boosted Decision Trees

788 The need of processing large quantities of data and discriminating between events with largely  
 789 similar experimental signatures makes multivariate statistical analysis (MVA) a largely used  
 790 method in the physics community. Multivariate classification methods based on machine  
 791 learning techniques are a fundamental ingredient to most analyses. The advantage of using  
 792 a MVA classifier is that it can achieve a better discrimination power with respect to a simple  
 793 cut and count analysis with a poorly discriminating variables. These variables are referred to  
 794 as weak variables and have similar distributions for signal and background samples. A risk of  
 795 using MVA classifiers is overtraining. This happens when there are too many model parameters  
 796 of an algorithm adjusted to too few data points. This leads to an increase in the classification  
 797 performance over the objectively achievable one.

798 There are many software tools that exist for MVA. In this thesis the Tool for Multivariate  
 799 Analysis (TMVA) [120] is used. This software is an open source project included into  
 800 ROOT [121]. All multivariate techniques in TMVA belong to supervised learning algorithms. By  
 801 training on events for which the outcome is known, a mapping function is determined that  
 802 describes a classification or an approximation of the underlying behaviour defining the target  
 803 value (regression).

804 In this thesis boosted decision trees (BDT) are employed for the classification of events as  
 805 implemented in the TMVA framework [120]. This multivariate technique is based on a set of  
 806 decision trees where each yields a binary output depending on the fact that an event is signal- or  
 807 background-like. The advantage of such a multivariate technique is that several discriminating  
 808 variables can be combined into a powerful one-dimensional discriminant D.

In Figure 3.4 a schematic view of a decision tree is shown. The starting point is the root node. Then a consecutive set of a total of  $i$  questions (nodes) regarding discriminating variables  $x_i$  are asked with only two possible answers per question (binary splits). The decision tree is constructed by training on a dataset for which the outcome is already provided, such as simulation dataset with signal and background processes (supervised learning). For each node a criterion  $x_i > C_i$  is found by maximizing the separation gain between nodes

$$\text{separationgain} \approx \text{gain}(\text{parent}) - \text{gain}(\text{daughter, Signal}) - \text{gain}(\text{daughter, Background}), \quad (3.7)$$

with the gain computed using the Gini index

$$\text{gain}(\text{cell}) \approx p(1-p), \quad (3.8)$$

809 where  $p$  denotes the purity of a selection  $x > C$ . This is repeated until the maximum of nodes is  
 810 reached and at the end of the sequence, the leaf nodes are labelled either signal S or background  
 811 B, depending on the majority of events that end up on those nodes.

Different trees can be combined into a forest where the final output is determined by the majority vote of all trees, forming the sum of so-called weak learners into one strong learner. From one training collection, trees are derived by reweighting events, and combined into a single classifier as the weighted average of each individual decision tree. A method for making such forests is boosting a tree. In this method, misclassified events are weighted higher so

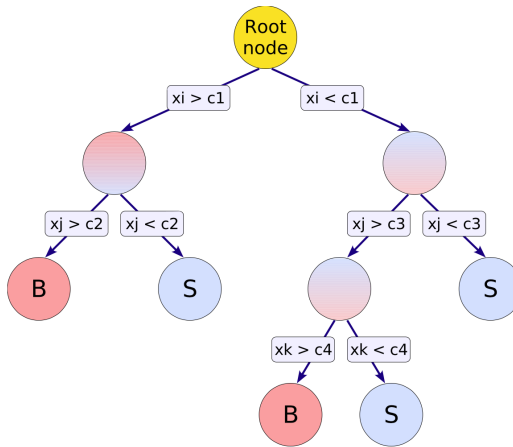


**Figure 3.4:** Schematic view of a decision tree. Figure taken from [120].

that future learner concentrate on these events. This has as advantage that the response of the decision trees are stabilised against fluctuations in the training sample which enhances the performance. Additionally, the trees can be kept very shallow, in this thesis  $i = 3$ , which improves the robustness against overtraining. Examples of such boosting algorithms are Adaptive Boosting (AdaBoost) and Gradient Boosting [122]. In AdaBoost, each weight of the misclassified events are enhanced while reducing the weight of correctly classified events after each training such that future events learn those better

$$\alpha_{n+1} = \left( \frac{1 - \epsilon_n}{\epsilon_n} \right)^\beta, \quad (3.9)$$

where  $\epsilon_n$  denotes the misclassification error of the current tree  $n$  and  $\beta$  is a learning rate. The weight  $w_i$  at node  $i$  is then equal to  $w_i = \ln \alpha_i$ . The final weight is the sum of all classifiers weighted by their errors. The learning rate is typically chosen to be  $\beta \leq 0.5$  to allow more boosting steps. Gradient boosting has a similar approach and combines a gradient descent with boosting. Instead of fitting the base-learner to the reweighted data as in AdaBoost, it is fitted to the negative gradient vector of the loss function evaluated at the previous node. Misclassified events will result in a majority vote with large gradients of the loss function. Also for the Gradient boost, the learning rate is typically slow, this also known as shrinkage. In this thesis Gradient boost is used with a shrinkage of 0.2-0.3.

In this thesis, the Gradient boost is used in combination with bagging, so-called stochastic gradient boosting. Bagging is a resampling technique draws a subset of events from the training data where the same event is allowed to be randomly picked several times from the parent sample. The tree is then trained on this subset and this is repeated many times. It is based on the assumption that sampling from a dataset that follows a distribution is the same as sampling from the distribution itself [123]. If one draws an event out of the parent sample, it is more likely to draw an event out of the phase space that has a high probability density, as the original dataset will have more events in the regions. Since the selected event is kept in the original sample, the parent sample stays unchanged so that randomly extracted samples have

830 the same parent distribution, albeit statistically fluctuated. Bagging smears over the statistical  
 831 fluctuations in the training data, making it suitable for stabilising the response of the classifier  
 832 and increasing the performance by eliminating overtraining. In stochastic gradient boosting the  
 833 bagging resampling procedure uses random sub-samples of the training events for growing the  
 834 trees.

835 The discriminating power of a BDT is assessed by analysing the receiver operating statistics  
 836 (ROC) curve. This curves show the background rejection over the signal efficiency of the  
 837 remaining sample. By looking at the area under the curve with respect to random guessing  
 838 (AUC), the best classifier can be identified. This follows the Neyman-Pearson lemma that  
 839 the best ROC curve is given by the likelihood ratio  $\mathcal{L}(x|Signal)/\mathcal{L}(x|Background)$  [123]. No  
 840 discrimination power will result in an AUC of 0%, while 50% means fully separated event  
 classes. In Figure ?? an example of ROC curve is shown.

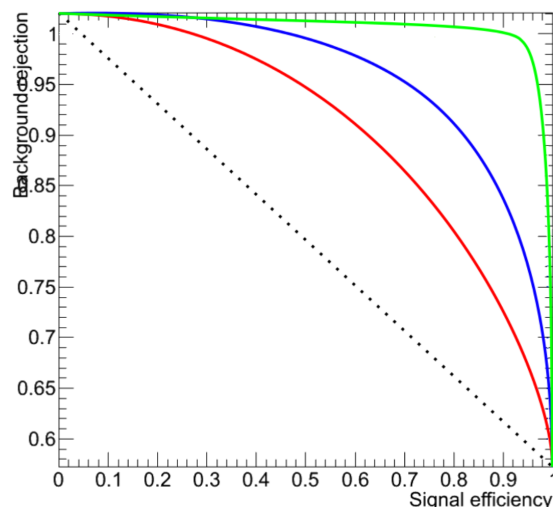


**Figure 3.5:** Example of ROC curves. In this example, the green method is better than the red one, which is better than the blue one. The dashed line represents a case where there is no separation. Figure taken from [124].

841

## 842 3.4 Template-based fitting

# Event reconstruction and selection

4

---

844 After the detector simulation described in Section ??, the simulated data has the exact same  
845 format as the real collision data recorded at the CMS experiment. Therefore the same software  
846 can be used for the reconstruction of both simulation and real data. In this Chapter, the event  
847 reconstruction for physics analysis is shown.

848 **4.1 Event reconstruction**

849 **4.2 Event selection**

850 **4.3 Regions and channels**

851 **4.4 Data driven background simulation**



# The search for FCNC involving a top quark and a Z boson

852

5

---

853 **5.1 Construction of template distributions**

854 **5.2 Systematic uncertainties**

855 **5.3 Limit setting procedure**

856 **5.4 Result and discussion**



# Conclusion and outlook

6

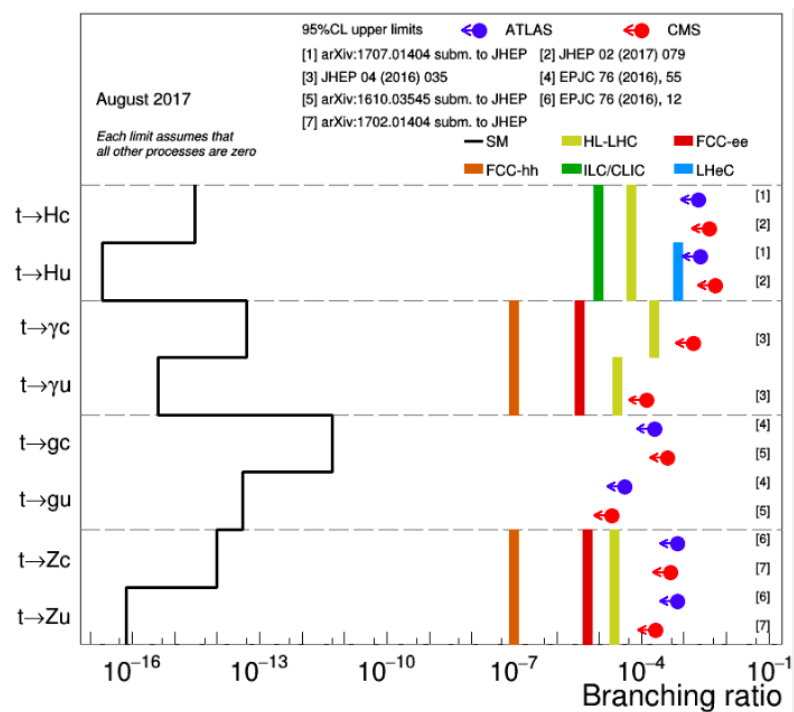


Figure 6.1:



# Bibliography

---

- 859 [1] MICHAEL E PESKIN and DANIEL V SCHROEDER: **An introduction to quantum field**  
 860 **theory; 1995 ed.** Includes exercises. Boulder, CO: Westview, 1995. URL: <https://cds.cern.ch/record/257493> (see pp. 1, 5).
- 861
- 862 [2] C. P. BURGESS: **Introduction to Effective Field Theory**. In: *Ann. Rev. Nucl. Part. Sci.*, **57**: (2007), pp. 329–362. DOI: [10.1146/annurev.nucl.56.080805.140508](https://doi.org/10.1146/annurev.nucl.56.080805.140508). arXiv: [hep-th/0701053 \[hep-th\]](https://arxiv.org/abs/hep-th/0701053) (see p. 1).
- 863
- 864
- 865 [3] NADIA ROBOTTI: **The discovery of the electron: I**. In: *European Journal of Physics*, **18**:3 (1997), p. 133. URL: <http://stacks.iop.org/0143-0807/18/i=3/a=002> (see p. 2).
- 866
- 867 [4] C. PATRIGNANI et al.: **Review of Particle Physics**. In: *Chin. Phys.*, **C40**:10 (2016),  
 868 p. 100001. DOI: [10.1088/1674-1137/40/10/100001](https://doi.org/10.1088/1674-1137/40/10/100001) (see pp. 2–3, 6–9, 34–35).
- 869
- 870 [5] S. ABACHI et al.: **Observation of the top quark**. In: *Phys. Rev. Lett.*, **74**: (1995),  
 871 pp. 2632–2637. DOI: [10.1103/PhysRevLett.74.2632](https://doi.org/10.1103/PhysRevLett.74.2632). arXiv: [hep-ex/9503003 \[hep-ex\]](https://arxiv.org/abs/hep-ex/9503003) (see p. 2).
- 872
- 873 [6] F. ABE et al.: **Observation of top quark production in  $\bar{p}p$  collisions**. In: *Phys. Rev. Lett.*, **74**: (1995), pp. 2626–2631. DOI: [10.1103/PhysRevLett.74.2626](https://doi.org/10.1103/PhysRevLett.74.2626). arXiv: [hep-ex/9503002 \[hep-ex\]](https://arxiv.org/abs/hep-ex/9503002) (see p. 2).
- 874
- 875 [7] SERGUEI CHATRHYAN et al.: **Observation of a new boson at a mass of 125 GeV with the CMS experiment at the LHC**. In: *Phys. Lett.*, **B716**: (2012), pp. 30–61. DOI:  
 876 [10.1016/j.physletb.2012.08.021](https://doi.org/10.1016/j.physletb.2012.08.021). arXiv: [1207.7235 \[hep-ex\]](https://arxiv.org/abs/1207.7235) (see pp. 2, 15).
- 877
- 878 [8] GEORGES AAD et al.: **Observation of a new particle in the search for the Standard Model Higgs boson with the ATLAS detector at the LHC**. In: *Phys. Lett.*, **B716**:  
 879 (2012), pp. 1–29. DOI: [10.1016/j.physletb.2012.08.020](https://doi.org/10.1016/j.physletb.2012.08.020). arXiv: [1207.7214 \[hep-ex\]](https://arxiv.org/abs/1207.7214) (see pp. 2, 15).
- 880
- 881
- 882 [9] NICOLA CABIBBO: **Unitary Symmetry and Leptonic Decays**. In: *Phys. Rev. Lett.*, **10**:  
 883 (12 June 1963), pp. 531–533. DOI: [10.1103/PhysRevLett.10.531](https://doi.org/10.1103/PhysRevLett.10.531) (see p. 5).
- 884
- 885 [10] S. L. GLASHOW, J. ILIOPoulos, and L. MAIANI: **Weak Interactions with Lepton-Hadron  
 886 Symmetry**. In: *Phys. Rev. D*, **2**: (7 Oct. 1970), pp. 1285–1292. DOI: [10.1103/PhysRevD.2.1285](https://doi.org/10.1103/PhysRevD.2.1285) (see p. 5).
- 887
- 888 [11] B.J. BJØRKEN and S.L. GLASHOW: **Elementary particles and SU(4)**. In: *Physics Letters*,  
 889 **11**:3 (1964), pp. 255–257. DOI: [https://doi.org/10.1016/0031-9163\(64\)90433-0](https://doi.org/10.1016/0031-9163(64)90433-0) (see p. 5).

- 890 [12] LUCIANO MAIANI: **The GIM Mechanism: origin, predictions and recent uses.** In: *Proceedings, 48th Rencontres de Moriond on Electroweak Interactions and Unified Theories: La Thuile, Italy, March 2-9, 2013.* 2013, pp. 3–16. arXiv: 1303.6154 [hep-ph]. URL: <https://inspirehep.net/record/1225307/files/arXiv:1303.6154.pdf> (see p. 5).
- 891 [13] PATRICK KOPPENBURG and SEBASTIEN DESCOTES-GENON: **The CKM Parameters.** In: (2017). arXiv: 1702.08834 [hep-ex] (see p. 6).
- 892 [14] J. A. AGUILAR-SAAVEDRA: **Top flavor-changing neutral interactions: Theoretical expectations and experimental detection.** In: *Acta Phys. Polon.*, B35: (2004), pp. 2695–2710. arXiv: hep-ph/0409342 [hep-ph] (see pp. 6, 11).
- 893 [15] YORIKIYO NAGASHIMA: **Beyond the standard model of elementary particle physics.** Weinheim, Germany: Wiley-VCH Verlag, 2014. URL: <http://www-spires.fnal.gov/spires/find/books/www?cl=QC793.2.N34::2014> (see p. 9).
- 894 [16] Y. FUKUDA et al.: **Evidence for oscillation of atmospheric neutrinos.** In: *Phys. Rev. Lett.*, 81: (1998), pp. 1562–1567. DOI: 10.1103/PhysRevLett.81.1562. arXiv: hep-ex/9807003 [hep-ex] (see p. 9).
- 895 [17] Y. ABE et al.: **Indication of Reactor  $\bar{\nu}_e$  Disappearance in the Double Chooz Experiment.** In: *Phys. Rev. Lett.*, 108: (13 Mar. 2012), p. 131801. DOI: 10.1103/PhysRevLett.108.131801 (see p. 9).
- 896 [18] P. A. R. ADE et al.: **Planck 2015 results. XIII. Cosmological parameters.** In: *Astron. Astrophys.*, 594: (2016), A13. DOI: 10.1051/0004-6361/201525830. arXiv: 1502.01589 [astro-ph.CO] (see p. 9).
- 897 [19] P. J. E. PEEBLES and BHARAT RATRA: **The Cosmological constant and dark energy.** In: *Rev. Mod. Phys.*, 75: (2003), pp. 559–606. DOI: 10.1103/RevModPhys.75.559. arXiv: astro-ph/0207347 [astro-ph] (see p. 9).
- 898 [20] A. D. SAKHAROV: **Violation of CP Invariance, c Asymmetry, and Baryon Asymmetry of the Universe.** In: *Pisma Zh. Eksp. Teor. Fiz.*, 5: (1967). [Usp. Fiz. Nauk 161, 61 (1991)], pp. 32–35. DOI: 10.1070/PU1991v034n05ABEH002497 (see p. 10).
- 899 [21] GUSTAVO BURDMAN: **New solutions to the hierarchy problem.** In: *Braz. J. Phys.*, 37: (2007), pp. 506–513. DOI: 10.1590/S0103-97332007000400006. arXiv: hep-ph/0703194 [hep-ph] (see p. 10).
- 900 [22] T. ET AL. AALTONEN: **Search for the Flavor-Changing Neutral-Current Decay  $t \rightarrow Zq$  in  $p\bar{p}$  Collisions at  $\sqrt{s} = 1.96$  TeV.** In: *Phys. Rev. Lett.*, 101: (19 Nov. 2008), p. 192002. DOI: 10.1103/PhysRevLett.101.192002 (see p. 11).
- 901 [23] VICTOR MUKHAMEDOVICH ABAZOV et al.: **Search for flavour changing neutral currents via quark-gluon couplings in single top quark production using  $2.3 \text{ fb}^{-1}$  of  $p\bar{p}$  collisions.** In: *Phys. Lett.*, B693: (2010), pp. 81–87. DOI: 10.1016/j.physletb.2010.08.011. arXiv: 1006.3575 [hep-ex] (see p. 11).
- 902 [24] GEORGES AAD et al.: **Search for flavour-changing neutral current top-quark decays to  $qZ$  in  $pp$  collision data collected with the ATLAS detector at  $\sqrt{s} = 8$  TeV.** In: *Eur. Phys. J.*, C76:1 (2016), p. 12. DOI: 10.1140/epjc/s10052-015-3851-5. arXiv: 1508.05796 [hep-ex] (see p. 11).

- 931 [25] GEORGES AAD et al.: **Search for single top-quark production via flavour-changing**  
 932 **neutral currents at 8 TeV with the ATLAS detector.** In: *Eur. Phys. J.*, **C76**:2 (2016),  
 933 p. 55. DOI: [10.1140/epjc/s10052-016-3876-4](https://doi.org/10.1140/epjc/s10052-016-3876-4). arXiv: [1509.00294](https://arxiv.org/abs/1509.00294) [hep-ex] (see pp. 11,  
 934 13).
- 935 [26] GEORGES AAD et al.: **Search for flavour-changing neutral current top quark decays**  
 936  **$t \rightarrow Hq$  in  $pp$  collisions at  $\sqrt{s} = 8$  TeV with the ATLAS detector.** In: *JHEP*, **12**:  
 937 (2015), p. 061. DOI: [10.1007/JHEP12\(2015\)061](https://doi.org/10.1007/JHEP12(2015)061). arXiv: [1509.06047](https://arxiv.org/abs/1509.06047) [hep-ex] (see  
 938 p. 11).
- 939 [27] MORAD AABOUD et al.: **Search for top quark decays  $t \rightarrow qH$ , with  $H \rightarrow \gamma\gamma$ , in**  
 940  **$\sqrt{s} = 13$  TeV  $pp$  collisions using the ATLAS detector.** In: (2017). arXiv: [1707.01404](https://arxiv.org/abs/1707.01404)  
 941 [hep-ex] (see pp. 11, 13).
- 942 [28] ALBERT M SIRUNYAN et al.: **Search for associated production of a Z boson with a**  
 943 **single top quark and for tZ flavour-changing interactions in  $pp$  collisions at  $\sqrt{s}$**   
 944 **= 8 TeV.** In: (2017). arXiv: [1702.01404](https://arxiv.org/abs/1702.01404) [hep-ex] (see pp. 11, 13).
- 945 [29] SERGUEI CHATRHYAN et al.: **Search for Flavor-Changing Neutral Currents in Top-**  
 946 **Quark Decays  $t \rightarrow Zq$  in  $pp$  Collisions at  $\sqrt{s} = 8$ TeV.** In: *Phys. Rev. Lett.*, **112**:17  
 947 (2014), p. 171802. DOI: [10.1103/PhysRevLett.112.171802](https://doi.org/10.1103/PhysRevLett.112.171802). arXiv: [1312.4194](https://arxiv.org/abs/1312.4194) [hep-ex]  
 948 (see p. 11).
- 949 [30] VARDAN KHACHATRYAN et al.: **Search for anomalous single top quark production in**  
 950 **association with a photon in  $pp$  collisions at  $\sqrt{s} = 8$  TeV.** In: *JHEP*, **04**: (2016),  
 951 p. 035. DOI: [10.1007/JHEP04\(2016\)035](https://doi.org/10.1007/JHEP04(2016)035). arXiv: [1511.03951](https://arxiv.org/abs/1511.03951) [hep-ex] (see pp. 11, 13).
- 952 [31] VARDAN KHACHATRYAN et al.: **Search for top quark decays via Higgs-boson-mediated**  
 953 **flavor-changing neutral currents in  $pp$  collisions at  $\sqrt{s} = 8$  TeV.** In: *JHEP*, **02**:  
 954 (2017), p. 079. DOI: [10.1007/JHEP02\(2017\)079](https://doi.org/10.1007/JHEP02(2017)079). arXiv: [1610.04857](https://arxiv.org/abs/1610.04857) [hep-ex] (see  
 955 p. 11).
- 956 [32] **Search for the flavor-changing interactions of the top quark with the Higgs boson**  
 957 **in  $H \rightarrow b\bar{b}$  channel at  $\sqrt{s} = 13$  TeV.** Tech. rep. CMS-PAS-TOP-17-003. Geneva:  
 958 CERN, 2017. URL: <https://cds.cern.ch/record/2284743> (see p. 11).
- 959 [33] J. A. AGUILAR-SAAVEDRA: **A Minimal set of top anomalous couplings.** In: *Nucl. Phys.*,  
 960 **B812**: (2009), pp. 181–204. DOI: [10.1016/j.nuclphysb.2008.12.012](https://doi.org/10.1016/j.nuclphysb.2008.12.012). arXiv: [0811.3842](https://arxiv.org/abs/0811.3842)  
 961 [hep-ph] (see p. 11).
- 962 [34] J. A. AGUILAR-SAAVEDRA: **A Minimal set of top-Higgs anomalous couplings.** In: *Nucl.*  
 963 *Phys.*, **B821**: (2009), pp. 215–227. DOI: [10.1016/j.nuclphysb.2009.06.022](https://doi.org/10.1016/j.nuclphysb.2009.06.022). arXiv:  
 964 [0904.2387](https://arxiv.org/abs/0904.2387) [hep-ph] (see p. 11).
- 965 [35] M. BENEKE et al.: **Top quark physics.** In: *1999 CERN Workshop on standard model*  
 966 *physics (and more) at the LHC, CERN, Geneva, Switzerland, 25-26 May: Proceedings.*  
 967 2000, pp. 419–529. arXiv: [hep-ph/0003033](https://arxiv.org/abs/hep-ph/0003033) [hep-ph]. URL: <http://weblib.cern.ch/abstract?CERN-TH-2000-100> (see p. 11).
- 968 [36] JUN GAO, CHONG SHENG LI, and HUA XING ZHU: **Top Quark Decay at Next-to-Next-**  
 969 **to Leading Order in QCD.** In: *Phys. Rev. Lett.*, **110**:4 (2013), p. 042001. DOI:  
 970 [10.1103/PhysRevLett.110.042001](https://doi.org/10.1103/PhysRevLett.110.042001). arXiv: [1210.2808](https://arxiv.org/abs/1210.2808) [hep-ph] (see p. 12).
- 971

- 972 [37] STEPHEN MYERS: **The LEP Collider, from design to approval and commissioning.**  
 973 John Adams' Lecture. Delivered at CERN, 26 Nov 1990. Geneva: CERN, 1991. URL:  
 974 <http://cds.cern.ch/record/226776> (see p. 15).
- 975 [38] STEPHEN HOLMES, RONALD S MOORE, and VLADIMIR SHILTSEV: **Overview of the**  
 976 **Tevatron collider complex: goals, operations and performance.** In: *Journal of In-*  
 977 *strumentation*, 6:08 (2011), T08001. URL: <http://stacks.iop.org/1748-0221/6/i=08/a=T08001> (see p. 15).
- 979 [39] R. BARATE et al.: **Search for the standard model Higgs boson at LEP.** In: *Phys.*  
 980 *Lett.*, B565: (2003), pp. 61–75. DOI: [10.1016/S0370-2693\(03\)00614-2](https://doi.org/10.1016/S0370-2693(03)00614-2). arXiv: [hep-ex/0306033 \[hep-ex\]](https://arxiv.org/abs/hep-ex/0306033) (see p. 15).
- 982 [40] KENNETH HERNER: **Higgs Boson Studies at the Tevatron.** In: *Nucl. Part. Phys. Proc.*,  
 983 273-275: (2016), pp. 852–856. DOI: [10.1016/j.nuclphysbps.2015.09.131](https://doi.org/10.1016/j.nuclphysbps.2015.09.131) (see p. 15).
- 984 [41] ABDELHAK DJOUADI: **The Anatomy of electro-weak symmetry breaking. I: The**  
 985 **Higgs boson in the standard model.** In: *Phys. Rept.*, 457: (2008), pp. 1–216. DOI:  
 986 [10.1016/j.physrep.2007.10.004](https://doi.org/10.1016/j.physrep.2007.10.004). arXiv: [hep-ph/0503172 \[hep-ph\]](https://arxiv.org/abs/hep-ph/0503172) (see p. 15).
- 987 [42] LYNDON EVANS and PHILIP BRYANT: **LHC Machine.** In: *Journal of Instrumentation*,  
 988 3:08 (2008), S08001. URL: <http://stacks.iop.org/1748-0221/3/i=08/a=S08001> (see  
 989 p. 15).
- 990 [43] THOMAS SVEN PETTERSSON and P LEFÈVRE: **The Large Hadron Collider: conceptual**  
 991 **design.** Tech. rep. CERN-AC-95-05-LHC. Oct. 1995, p. 20 and 22. URL: <https://cds.cern.ch/record/291782> (see p. 15).
- 993 [44] JORG WENNINGER and EZIO TODESCO: **Large Hadron Collider momentum calibration**  
 994 **and accuracy.** Tech. rep. CERN-ACC-2017-0007. Geneva: CERN, Feb. 2017. URL:  
 995 <https://cds.cern.ch/record/2254678> (see p. 16).
- 996 [45] CINZIA DE MELIS: **The CERN accelerator complex. Complexe des accélérateurs du**  
 997 **CERN.** In: (July 2016). General Photo. URL: <https://cds.cern.ch/record/2197559>  
 998 (see p. 16).
- 999 [46] OLIVER SIM BRÜNING, PAUL COLLIER, P LEBRUN, et al.: **LHC Design Report.** CERN  
 1000 Yellow Reports: Monographs. Geneva: CERN, 2004. URL: <https://cds.cern.ch/record/782076> (see p. 16).
- 1002 [47] G. AAD et al.: **The ATLAS Experiment at the CERN Large Hadron Collider.** In: *JINST*,  
 1003 3: (2008), S08003. DOI: [10.1088/1748-0221/3/08/S08003](https://doi.org/10.1088/1748-0221/3/08/S08003) (see p. 17).
- 1004 [48] S. CHATRCHYAN et al.: **The CMS Experiment at the CERN LHC.** In: *JINST*, 3: (2008),  
 1005 S08004. DOI: [10.1088/1748-0221/3/08/S08004](https://doi.org/10.1088/1748-0221/3/08/S08004) (see pp. 17, 26–27).
- 1006 [49] K. AAMODT et al.: **The ALICE experiment at the CERN LHC.** In: *JINST*, 3: (2008),  
 1007 S08002. DOI: [10.1088/1748-0221/3/08/S08002](https://doi.org/10.1088/1748-0221/3/08/S08002) (see p. 17).
- 1008 [50] A. AUGUSTO ALVES JR. et al.: **The LHCb Detector at the LHC.** In: *JINST*, 3: (2008),  
 1009 S08005. DOI: [10.1088/1748-0221/3/08/S08005](https://doi.org/10.1088/1748-0221/3/08/S08005) (see p. 17).
- 1010 [51] M. BONGI et al.: **Astroparticle physics at LHC: The LHCf experiment ready for data**  
 1011 **taking.** In: *Nucl. Instrum. Meth.*, A612: (2010), pp. 451–454. DOI: [10.1016/j.nima.2009.08.039](https://doi.org/10.1016/j.nima.2009.08.039) (see p. 17).

- 1013 [52] G. ANELLI et al.: **The TOTEM experiment at the CERN Large Hadron Collider**. In: *JINST*, 3: (2008), S08007. doi: [10.1088/1748-0221/3/08/S08007](https://doi.org/10.1088/1748-0221/3/08/S08007) (see p. 17).
- 1014
- 1015 [53] B. ACHARYA et al.: **The Physics Programme Of The MoEDAL Experiment At The LHC**.  
1016 In: *Int. J. Mod. Phys.*, A29: (2014), p. 1430050. doi: [10.1142/S0217751X14300506](https://doi.org/10.1142/S0217751X14300506).  
1017 arXiv: [1405.7662 \[hep-ph\]](https://arxiv.org/abs/1405.7662) (see p. 17).
- 1018 [54] BY JAMES GILLIES: **Luminosity? Why don't we just say collision rate?** In: (Mar.  
1019 2011). URL: <http://cds.cern.ch/record/1997001> (see p. 17).
- 1020 [55] BY HARRIET JARLETT and HARRIET KIM JARLETT: **LHC pushes limits of performance**.  
1021 In: (Aug. 2016). URL: <http://cds.cern.ch/record/2212301> (see p. 18).
- 1022 [56] **Technical proposal.** LHC Tech. Proposal. Cover title : CMS, the Compact Muon  
1023 Solenoid : technical proposal. Geneva: CERN, 1994. URL: [https://cds.cern.ch/](https://cds.cern.ch/record/290969)  
1024 [record/290969](https://cds.cern.ch/record/290969) (see p. 18).
- 1025 [57] G. L. BAYATIAN et al.: **CMS physics: Technical design report**. In: (2006) (see pp. 18,  
1026 28).
- 1027 [58] G L BAYATIAN, S CHATRCHYAN, G HMAYAKYAN, et al.: **CMS Physics: Technical Design  
1028 Report Volume 1: Detector Performance and Software**. Technical Design Report  
1029 CMS. There is an error on cover due to a technical problem for some items. Geneva:  
1030 CERN, 2006. URL: <https://cds.cern.ch/record/922757> (see pp. 18, 25, 30).
- 1031 [59] BY CIAN O'LUANAIGH: **LHC progresses towards higher intensities**. In: (Aug. 2015).  
1032 URL: <http://cds.cern.ch/record/2051986> (see p. 19).
- 1033 [60] CMS COLLABORATION: **Detector Drawings**. CMS Collection. Mar. 2012. URL: <https://cds.cern.ch/record/1433717> (see p. 19).
- 1034
- 1035 [61] BY CORINNE PRALAVORIO and CORINNE PRALAVORIO: **Major work to ready the LHC  
1036 experiments for Run 2**. In: (May 2015). URL: <http://cds.cern.ch/record/2024977>  
1037 (see pp. 19, 30).
- 1038 [62] S CHATRCHYAN, V KHACHATRYAN, A M SIRUNYAN, et al.: **Performance of the CMS Drift  
1039 Tube Chambers with Cosmic Rays**. In: *J. Instrum.*, 5:arXiv:0911.4855. CMS-CFT-  
1040 09-012 (Nov. 2009), T03015 . 47 p. URL: <http://cds.cern.ch/record/1223944> (see  
1041 pp. 22–23).
- 1042 [63] LUIGI GUIDUCCI: **CMS muon system towards LHC Run 2 and beyond**. Tech. rep.  
1043 CMS-CR-2014-333. Geneva: CERN, Oct. 2014. URL: [https://cds.cern.ch/record/](https://cds.cern.ch/record/1966038)  
1044 [1966038](https://cds.cern.ch/record/1966038) (see p. 24).
- 1045 [64] CARLO BATTILANA: **The CMS muon system status and upgrades for LHC run-2 and  
1046 performance of muon reconstruction with 13 TeV data**. Tech. rep. CMS-CR-2016-  
1047 437. Geneva: CERN, Dec. 2016. URL: <http://cds.cern.ch/record/2239185> (see  
1048 p. 24).
- 1049 [65] SERGUEI CHATRCHYAN et al.: **Performance of CMS muon reconstruction in  $pp$  col-  
1050 lision events at  $\sqrt{s} = 7$  TeV**. In: *JINST*, 7: (2012), P10002. doi: [10.1088/1748-0221/7/10/P10002](https://doi.org/10.1088/1748-0221/7/10/P10002). arXiv: [1206.4071 \[physics.ins-det\]](https://arxiv.org/abs/1206.4071) (see p. 24).
- 1051

- 1052 [66] R. FRÜHWIRTH: **Application of Kalman filtering to track and vertex fitting**. In: *Nuclear Instruments and Methods in Physics Research Section A: Accelerators, Spectrometers, Detectors and Associated Equipment*, **262**:2 (1987), pp. 444–450. doi: [http://dx.doi.org/10.1016/0168-9002\(87\)90887-4](http://dx.doi.org/10.1016/0168-9002(87)90887-4) (see pp. 24, 30).
- 1053  
1054  
1055
- 1056 [67] PIERRE BILLOIR: **Progressive track recognition with a Kalman like fitting procedure**. In: *Comput. Phys. Commun.*, **57**: (1989), pp. 390–394. doi: [10.1016/0010-4655\(89\)90249-X](10.1016/0010-4655(89)90249-X) (see pp. 24, 30).
- 1057  
1058
- 1059 [68] EMRAH TIRAS, BURAK BILKI, and YASAR ONEL: **Commissioning of CMS Forward Hadron Calorimeters with Upgraded Multi-anode PMTs and μTCA Readout**. In: (2016). arXiv: [1611.05232 \[physics.ins-det\]](1611.05232) (see p. 25).
- 1060  
1061
- 1062 [69] L. BRIANZA: **Precision crystal calorimetry in LHC Run II with the CMS ECAL**. In: *Journal of Instrumentation*, **12**:01 (2017), p. C01069. URL: <http://stacks.iop.org/1748-0221/12/i=01/a=C01069> (see pp. 27–28).
- 1063  
1064
- 1065 [70] SERGUEI CHATRCHYAN et al.: **Energy Calibration and Resolution of the CMS Electromagnetic Calorimeter in  $pp$  Collisions at  $\sqrt{s} = 7$  TeV**. In: *JINST*, **8**: (2013). [*JINST8,9009(2013)*], P09009. doi: <10.1088/1748-0221/8/09/P09009>. arXiv: [1306.2016 \[hep-ex\]](1306.2016) (see p. 28).
- 1066  
1067  
1068
- 1069 [71] SERGUEI CHATRCHYAN, VARDAN KHACHATRYAN, ALBERT M SIRUNYAN, et al.: **Description and performance of track and primary-vertex reconstruction with the CMS tracker**. In: *J. Instrum.*, **9**:arXiv:1405.6569. CERN-PH-EP-2014-070. CMS-TRK-11-001 (May 2014). Comments: Replaced with published version. Added journal reference and DOI, P10009. 80 p. URL: <http://cds.cern.ch/record/1704291> (see pp. 28, 31).
- 1070  
1071  
1072  
1073
- 1074 [72] BY CHRISTINE SUTTON: **Chronicles of CMS: the saga of LS1**. In: (May 2015). URL: <http://cds.cern.ch/record/2024986> (see p. 29).
- 1075
- 1076 [73] **A beautiful barrel for CMS**. In: (Mar. 2014). URL: <http://cds.cern.ch/record/1998635> (see p. 29).
- 1077
- 1078 [74] **Cool running for CMS tracker**. In: (Mar. 2014). URL: <http://cds.cern.ch/record/1998606> (see p. 30).
- 1079
- 1080 [75] K. ROSE: **Deterministic annealing for clustering, compression, classification, regression, and related optimization problems**. In: *Proceedings of the IEEE*, **86**:11 (Nov. 1998), pp. 2210–2239. doi: <10.1109/5.726788> (see p. 31).
- 1081  
1082
- 1083 [76] WOLFGANG WALTENBERGER: **Adaptive Vertex Reconstruction**. Tech. rep. CMS-NOTE-2008-033. Geneva: CERN, July 2008. URL: <https://cds.cern.ch/record/1166320> (see p. 31).
- 1084  
1085
- 1086 [77] L. CADAMURO: **The CMS Level-1 trigger system for LHC Run II**. In: *Journal of Instrumentation*, **12**:03 (2017), p. C03021. URL: <http://stacks.iop.org/1748-0221/12/i=03/a=C03021> (see p. 31).
- 1087  
1088
- 1089 [78] VARDAN KHACHATRYAN et al.: **The CMS trigger system**. In: *JINST*, **12**:01 (2017), P01020. doi: <10.1088/1748-0221/12/01/P01020>. arXiv: [1609.02366 \[physics.ins-det\]](1609.02366) (see p. 32).
- 1090  
1091

- 1092 [79] CLAUDIO GRANDI, DAVID STICKLAND, LUCAS TAYLOR, ACHILLE PETRILLI, and ALAIN  
 1093 HERVÉ: **CMS Computing Model: The "CMS Computing Model RTAG"**. Tech. rep.  
 1094 CMS-NOTE-2004-031. CERN-LHCC-2004-035. LHCC-G-083. Geneva: CERN, Dec.  
 1095 2004. URL: <http://cds.cern.ch/record/814248> (see p. 32).
- 1096 [80] CHRISTOPH ECK, J KNOBLOCH, LESLIE ROBERTSON, et al.: **LHC computing Grid: Technical**  
 1097 **Design Report. Version 1.06 (20 Jun 2005)**. Technical Design Report LCG.  
 1098 Geneva: CERN, 2005. URL: <https://cds.cern.ch/record/840543> (see p. 32).
- 1099 [81] JOHN C. COLLINS, DAVISON E. SOPER, and GEORGE F. STERMAN: **Factorization of Hard**  
 1100 **Processes in QCD**. In: *Adv. Ser. Direct. High Energy Phys.*, 5: (1989), pp. 1–91. DOI:  
 1101 [10.1142/9789814503266\\_0001](https://doi.org/10.1142/9789814503266_0001). arXiv: [hep-ph/0409313 \[hep-ph\]](https://arxiv.org/abs/hep-ph/0409313) (see p. 33).
- 1102 [82] RINGAILE PLACAKYTE: **Parton Distribution Functions**. In: *Proceedings, 31st International Conference on Physics in collisions (PIC 2011): Vancouver, Canada, August 28-September 1, 2011*. 2011. arXiv: [1111.5452 \[hep-ph\]](https://arxiv.org/abs/1111.5452). URL: <https://inspirehep.net/record/954990/files/arXiv:1111.5452.pdf> (see p. 33).
- 1106 [83] RICHARD D. BALL, VALERIO BERTONE, STEFANO CARRAZZA, et al.: **Parton distributions**  
 1107 **for the LHC run II**. In: *Journal of High Energy Physics*, 2015:4 (2015), p. 40. DOI:  
 1108 [10.1007/JHEP04\(2015\)040](https://doi.org/10.1007/JHEP04(2015)040) (see p. 33).
- 1109 [84] JON BUTTERWORTH et al.: **PDF4LHC recommendations for LHC Run II**. In: *J. Phys.*,  
 1110 **G43**: (2016), p. 023001. DOI: [10.1088/0954-3899/43/2/023001](https://doi.org/10.1088/0954-3899/43/2/023001). arXiv: [1510.03865](https://arxiv.org/abs/1510.03865)  
 1111 [hep-ph] (see pp. 33–34).
- 1112 [85] H. ABRAMOWICZ and A. CALDWELL: **HERA collider physics**. In: *Rev. Mod. Phys.*, 71:  
 1113 (1999), pp. 1275–1410. DOI: [10.1103/RevModPhys.71.1275](https://doi.org/10.1103/RevModPhys.71.1275). arXiv: [hep-ex/9903037](https://arxiv.org/abs/hep-ex/9903037)  
 1114 [hep-ex] (see p. 33).
- 1115 [86] STEPHEN HOLMES, RONALD S. MOORE, and VLADIMIR SHILTSEV: **Overview of the Tevatron**  
 1116 **Collider Complex: Goals, Operations and Performance**. In: *JINST*, 6: (2011),  
 1117 T08001. DOI: [10.1088/1748-0221/6/08/T08001](https://doi.org/10.1088/1748-0221/6/08/T08001). arXiv: [1106.0909 \[physics.acc-ph\]](https://arxiv.org/abs/1106.0909)  
 1118 (see p. 33).
- 1119 [87] JUAN ROJO et al.: **The PDF4LHC report on PDFs and LHC data: Results from Run I**  
 1120 **and preparation for Run II**. In: *J. Phys.*, **G42**: (2015), p. 103103. DOI: [10.1088/0954-3899/42/10/103103](https://doi.org/10.1088/0954-3899/42/10/103103). arXiv: [1507.00556 \[hep-ph\]](https://arxiv.org/abs/1507.00556) (see p. 33).
- 1122 [88] J. PUMPLIN, D. STUMP, R. BROCK, et al.: **Uncertainties of predictions from parton**  
 1123 **distribution functions. 2. The Hessian method**. In: *Phys. Rev.*, **D65**: (2001), p. 014013.  
 1124 DOI: [10.1103/PhysRevD.65.014013](https://doi.org/10.1103/PhysRevD.65.014013). arXiv: [hep-ph/0101032 \[hep-ph\]](https://arxiv.org/abs/hep-ph/0101032) (see p. 34).
- 1125 [89] FRANZ MANDL and GRAHAM G SHAW: **Quantum field theory; 2nd ed.** New York, NY:  
 1126 Wiley, 2010. URL: [https://cds.cern.ch/record/1236742](http://cds.cern.ch/record/1236742) (see p. 35).
- 1127 [90] S BANERJEE: **CMS Simulation Software**. In: *Journal of Physics: Conference Series*,  
 1128 **396**:2 (2012), p. 022003. URL: <http://stacks.iop.org/1742-6596/396/i=2/a=022003>  
 1129 (see p. 36).
- 1130 [91] M HILDRETH, V N IVANCHENKO, D J LANGE, and M J KORTELAINEN: **CMS Full Simu-**  
 1131 **lation for Run-2**. In: *Journal of Physics: Conference Series*, **664**:7 (2015), p. 072022.  
 1132 URL: <http://stacks.iop.org/1742-6596/664/i=7/a=072022> (see p. 36).

- 1133 [92] S. AGOSTINELLI, J. ALLISON, K. AMAKO, et al.: **Geant4-a simulation toolkit**. In: *Nuclear*  
 1134 *Instruments and Methods in Physics Research Section A: Accelerators, Spectrometers,*  
 1135 *Detectors and Associated Equipment*, **506**:3 (2003), pp. 250–303. doi: [https://doi.org/10.1016/S0168-9002\(03\)01368-8](https://doi.org/10.1016/S0168-9002(03)01368-8) (see pp. 36, 38).
- 1137 [93] MICHAEL H. SEYMOUR and MARILYN MARX: **Monte Carlo Event Generators**. In: *Proceedings, 69th Scottish Universities Summer School in Physics : LHC Phenomenology (SUSSP69): St.Andrews, Scotland, August 19-September 1, 2012.* 2013, pp. 287–319.  
 1138 doi: [10.1007/978-3-319-05362-2\\_8](10.1007/978-3-319-05362-2_8). arXiv: <1304.6677> [hep-ph] (see p. 36).
- 1141 [94] TORBJORN SJÖSTRAND: **Monte Carlo Tools**. In: *Proceedings, 65th Scottish Universities*  
 1142 *Summer School in Physics: LHC Physics (SUSSP65): St. Andrews, UK, August 16-29,*  
 1143 *2009.* 2009, pp. 309–339. doi: <10.1201/b11865-14>. arXiv: <0911.5286> [hep-ph] (see  
 1144 p. 36).
- 1145 [95] STEFAN HÖCHE: **Introduction to parton-shower event generators**. In: *Proceedings, Theoretical Advanced Study Institute in Elementary Particle Physics: Journeys Through the Precision Frontier: Amplitudes for Colliders (TASI 2014): Boulder, Colorado, June 2-27, 2014.* 2015, pp. 235–295. doi: [10.1142/9789814678766\\_0005](10.1142/9789814678766_0005). arXiv: <1411.4085> [hep-ph] (see p. 36).
- 1150 [96] ADAM ALLOUL, NEIL D. CHRISTENSEN, CELINE DEGRANDE, CLAUDE DUHR, and BEN-  
 1151 JAMIN FUKS: **FeynRules 2.0 - A complete toolbox for tree-level phenomenology**. In:  
 1152 *Comput. Phys. Commun.*, **185**: (2014), pp. 2250–2300. doi: <10.1016/j.cpc.2014.04.012>. arXiv: <1310.1921> [hep-ph] (see p. 37).
- 1154 [97] CELINE DEGRANDE, CLAUDE DUHR, BENJAMIN FUKS, et al.: **UFO - The Universal**
- 1155 **FeynRules Output**. In: *Comput. Phys. Commun.*, **183**: (2012), pp. 1201–1214. doi:  
 1156 <10.1016/j.cpc.2012.01.022>. arXiv: <1108.2040> [hep-ph] (see p. 37).
- 1157 [98] JOHAN ALWALL, MICHEL HERQUET, FABIO MALTONI, OLIVIER MATTELAER, and TIM  
 1158 STELZER: **MadGraph 5 : Going Beyond**. In: *JHEP*, **06**: (2011), p. 128. doi: [10.1007/JHEP06\(2011\)128](10.1007/JHEP06(2011)128). arXiv: <1106.0522> [hep-ph] (see pp. 37, 40).
- 1160 [99] MICHELANGELO L. MANGANO, MAURO MORETTI, FULVIO PICCININI, and MICHELE TREC-  
 1161 CANI: **Matching matrix elements and shower evolution for top-quark production**  
 1162 **in hadronic collisions**. In: *JHEP*, **01**: (2007), p. 013. doi: <10.1088/1126-6708/2007/01/013>. arXiv: <hep-ph/0611129> [hep-ph] (see p. 37).
- 1164 [100] TORBJORN SJOSTRAND, STEFAN ASK, JESPER R. CHRISTIANSEN, et al.: **An introduction**  
 1165 **to {PYTHIA} 8.2**. In: *Computer Physics Communications*, **191**: (2015), pp. 159–177.  
 1166 doi: <http://dx.doi.org/10.1016/j.cpc.2015.01.024> (see p. 37).
- 1167 [101] TORBJORN SJOSTRAND, STEPHEN MRENNA, and PETER Z. SKANDS: **PYTHIA 6.4 Physics**  
 1168 **and Manual**. In: *JHEP*, **0605**: (2006), p. 026. doi: <10.1088/1126-6708/2006/05/026>.  
 1169 arXiv: <hep-ph/0603175> [hep-ph] (see p. 37).
- 1170 [102] TORBJORN SJOSTRAND, STEFAN ASK, JESPER R. CHRISTIANSEN, et al.: **An Introduction**  
 1171 **to PYTHIA 8.2**. In: *Comput. Phys. Commun.*, **191**: (2015), pp. 159–177. doi:  
 1172 <10.1016/j.cpc.2015.01.024>. arXiv: <1410.3012> [hep-ph] (see pp. 37, 39).

- 1173 [103] JOHAN ALWALL et al.: **Comparative study of various algorithms for the merging**  
1174 **of parton showers and matrix elements in hadronic collisions.** In: *Eur. Phys. J.*,  
1175 **C53:** (2008), pp. 473–500. doi: [10.1140/epjc/s10052-007-0490-5](https://doi.org/10.1140/epjc/s10052-007-0490-5). arXiv: [0706.2569](https://arxiv.org/abs/0706.2569)  
1176 [[hep-ph](#)] (see p. 37).
- 1177 [104] J. ALWALL, R. FREDERIX, S. FRIXIONE, et al.: **The automated computation of tree-level**  
1178 **and next-to-leading order differential cross sections, and their matching to parton**  
1179 **shower simulations.** In: *JHEP*, **07:** (2014), p. 079. doi: [10.1007/JHEP07\(2014\)079](https://doi.org/10.1007/JHEP07(2014)079).  
1180 arXiv: [1405.0301](https://arxiv.org/abs/1405.0301) [[hep-ph](#)] (see pp. 37, 40).
- 1181 [105] RIKKERT FREDERIX and STEFANO FRIXIONE: **Merging meets matching in MC@NLO.**  
1182 In: *JHEP*, **12:** (2012), p. 061. doi: [10.1007/JHEP12\(2012\)061](https://doi.org/10.1007/JHEP12(2012)061). arXiv: [1209.6215](https://arxiv.org/abs/1209.6215)  
1183 [[hep-ph](#)] (see p. 37).
- 1184 [106] SIMONE ALIOLI, PAOLO NASON, CARLO OLEARI, and EMANUELE RE: **A general frame-**  
1185 **work for implementing NLO calculations in shower Monte Carlo programs: the**  
1186 **POWHEG BOX.** In: *Journal of High Energy Physics*, **2010**:6 (2010), p. 43. doi: [10.1007/JHEP06\(2010\)043](https://doi.org/10.1007/JHEP06(2010)043) (see p. 37).
- 1188 [107] SIMONE ALIOLI, PAOLO NASON, CARLO OLEARI, and EMANUELE RE: **NLO single-top**  
1189 **production matched with shower in POWHEG: s - and t -channel contributions.**  
1190 In: *Journal of High Energy Physics*, **2009**:09 (2009), p. 111. url: <http://stacks.iop.org/1126-6708/2009/i=09/a=111> (see p. 37).
- 1192 [108] STEFANO FRIXIONE, PAOLO NASON, and CARLO OLEARI: **Matching NLO QCD com-**  
1193 **putations with parton shower simulations: the POWHEG method.** In: *Journal of*  
1194 *High Energy Physics*, **2007**:11 (2007), p. 070. url: <http://stacks.iop.org/1126-6708/2007/i=11/a=070> (see p. 37).
- 1196 [109] SIMONE ALIOLI, PAOLO NASON, CARLO OLEARI, and EMANUELE RE: **A general frame-**  
1197 **work for implementing NLO calculations in shower Monte Carlo programs: the**  
1198 **POWHEG BOX.** In: *JHEP*, **06:** (2010), p. 043. doi: [10.1007/JHEP06\(2010\)043](https://doi.org/10.1007/JHEP06(2010)043). arXiv: [1002.2581](https://arxiv.org/abs/1002.2581) [[hep-ph](#)] (see p. 37).
- 1200 [110] STEFANO FRIXIONE, PAOLO NASON, and CARLO OLEARI: **Matching NLO QCD com-**  
1201 **putations with Parton Shower simulations: the POWHEG method.** In: *JHEP*, **11:**  
1202 (2007), p. 070. doi: [10.1088/1126-6708/2007/11/070](https://doi.org/10.1088/1126-6708/2007/11/070). arXiv: [0709.2092](https://arxiv.org/abs/0709.2092) [[hep-ph](#)] (see  
1203 p. 37).
- 1204 [111] PAOLO NASON: **A New method for combining NLO QCD with shower Monte Carlo**  
1205 **algorithms.** In: *JHEP*, **11:** (2004), p. 040. doi: [10.1088/1126-6708/2004/11/040](https://doi.org/10.1088/1126-6708/2004/11/040).  
1206 arXiv: [hep-ph/0409146](https://arxiv.org/abs/hep-ph/0409146) [[hep-ph](#)] (see p. 37).
- 1207 [112] ANDREI V. GRITSAN, RAOUL RÖNTSCH, MARKUS SCHULZE, and MENG XIAO: **Constraining**  
1208 **anomalous Higgs boson couplings to the heavy flavor fermions using matrix**  
1209 **element techniques.** In: *Phys. Rev.*, **D94**:5 (2016), p. 055023. doi: [10.1103/PhysRevD.94.055023](https://doi.org/10.1103/PhysRevD.94.055023). arXiv: [1606.03107](https://arxiv.org/abs/1606.03107) [[hep-ph](#)] (see pp. 37, 40).
- 1211 [113] IAN ANDERSON et al.: **Constraining anomalous HVV interactions at proton and**  
1212 **lepton colliders.** In: *Phys. Rev.*, **D89**:3 (2014), p. 035007. doi: [10.1103/PhysRevD.89.035007](https://doi.org/10.1103/PhysRevD.89.035007). arXiv: [1309.4819](https://arxiv.org/abs/1309.4819) [[hep-ph](#)] (see pp. 37, 40).

- 1214 [114] SARA BOLOGNESI, YANYAN GAO, ANDREI V. GRITSAN, et al.: **On the spin and parity of**  
 1215 **a single-produced resonance at the LHC.** In: *Phys. Rev.*, **D86**: (2012), p. 095031.  
 1216 DOI: [10.1103/PhysRevD.86.095031](https://doi.org/10.1103/PhysRevD.86.095031). arXiv: [1208.4018 \[hep-ph\]](https://arxiv.org/abs/1208.4018) (see pp. 37, 40).
- 1217 [115] YANYAN GAO, ANDREI V. GRITSAN, ZIJIN GUO, et al.: **Spin determination of single-**  
 1218 **produced resonances at hadron colliders.** In: *Phys. Rev.*, **D81**: (2010), p. 075022.  
 1219 DOI: [10.1103/PhysRevD.81.075022](https://doi.org/10.1103/PhysRevD.81.075022). arXiv: [1001.3396 \[hep-ph\]](https://arxiv.org/abs/1001.3396) (see pp. 37, 40).
- 1220 [116] PIERRE ARTOISENET, RIKKERT FREDERIX, OLIVIER MATTELAER, and ROBBERT RIETK-  
 1221 ERK: **Automatic spin-entangled decays of heavy resonances in Monte Carlo simula-**  
 1222 **tions.** In: *JHEP*, **03**: (2013), p. 015. doi: [10.1007/JHEP03\(2013\)015](https://doi.org/10.1007/JHEP03(2013)015). arXiv: [1212.3460](https://arxiv.org/abs/1212.3460)  
 1223 [hep-ph] (see pp. 37, 40).
- 1224 [117] V. KHACHATRYAN and ETAL: **Event generator tunes obtained from underlying event**  
 1225 **and multiparton scattering measurements.** In: *The European Physical Journal C*,  
 1226 **76**:3 (Mar. 17, 2016), p. 155. doi: [10.1140/epjc/s10052-016-3988-x](https://doi.org/10.1140/epjc/s10052-016-3988-x) (see p. 38).
- 1227 [118] J. PUMPLIN, D. R. STUMP, J. HUSTON, et al.: **New generation of parton distributions**  
 1228 **with uncertainties from global QCD analysis.** In: *JHEP*, **07**: (2002), p. 012. doi:  
 1229 [10.1088/1126-6708/2002/07/012](https://doi.org/10.1088/1126-6708/2002/07/012). arXiv: [hep-ph/0201195 \[hep-ph\]](https://arxiv.org/abs/hep-ph/0201195) (see p. 38).
- 1230 [119] YUE ZHANG, Bo HUA LI, CHONG SHENG LI, JUN GAO, and HUA XING ZHU: **Next-to-**  
 1231 **leading order QCD corrections to the top quark associated with  $\gamma$  production via**  
 1232 **model-independent flavor-changing neutral-current couplings at hadron collid-**  
 1233 **ers.** In: *Phys. Rev.*, **D83**: (2011), p. 094003. doi: [10.1103/PhysRevD.83.094003](https://doi.org/10.1103/PhysRevD.83.094003). arXiv:  
 1234 [1101.5346 \[hep-ph\]](https://arxiv.org/abs/1101.5346) (see p. 39).
- 1235 [120] A. HOECKER, P. SPECKMAYER, J. STELZER, et al.: **TMVA - Toolkit for Multivariate**  
 1236 **Data Analysis.** In: *ArXiv Physics e-prints*, (Mar. 2007). eprint: [physics/0703039](https://arxiv.org/abs/physics/0703039) (see  
 1237 pp. 42–43).
- 1238 [121] R. BRUN and F. RADEMAKERS: **ROOT: An object oriented data analysis framework.**  
 1239 In: *Nucl. Instrum. Meth.*, **A389**: (1997), pp. 81–86. doi: [10.1016/S0168-9002\(97\)](https://doi.org/10.1016/S0168-9002(97)00048-X)  
 1240 [00048-X](https://arxiv.org/abs/00048-X) (see p. 42).
- 1241 [122] A. MAYR, H. BINDER, O. GEFELLER, and M. SCHMID: **The Evolution of Boosting**  
 1242 **Algorithms - From Machine Learning to Statistical Modelling.** In: *ArXiv e-prints*,  
 1243 (Mar. 2014). arXiv: [1403.1452 \[stat.ME\]](https://arxiv.org/abs/1403.1452) (see p. 43).
- 1244 [123] OLAF BEHNKE, KEVIN KRONINGER, GREGORY SCHOTT, and THOMAS SCHORNER-SADENIUS ■  
 1245 **Data Analysis in High Energy Physics: A Practical Guide to Statistical Methods.** 1st.  
 1246 Wiley-VCH, 2013 (see pp. 43–44).
- 1247 [124] (see p. 44).